

# Exploring the connection between AGN radiative feedback and massive black hole spin

F. Bollati<sup>1,2,\*</sup>, A. Lupi<sup>1,2,3</sup>, M. Dotti<sup>3,2,4</sup>, and F. Haardt<sup>1,2,4</sup>

<sup>1</sup> DiSAT, Università degli Studi dell'Insubria, via Valleggio 11, I-22100 Como, Italy

<sup>2</sup> INFN, Sezione di Milano-Bicocca, Piazza della Scienza 3, I-20126 Milano, Italy

<sup>3</sup> Dipartimento di Fisica G. Occhialini, Università di Milano-Bicocca, Piazza della Scienza 3, I-20126 Milano, Italy

<sup>4</sup> INAF, Osservatorio Astronomico di Brera, Via E. Bianchi 46, I-23807 Merate, Italy

Received 9 November 2023 / Accepted 15 April 2024

## ABSTRACT

We present a novel implementation for active galactic nucleus (AGN) feedback through ultrafast winds in the code GIZMO. Our feedback recipe accounts for the angular dependence of radiative feedback on black hole spin. We self-consistently evolve in time (i) the gas-accretion process from resolved scales to a smaller scale unresolved (subgrid) AGN disk, (ii) the evolution of the spin of the massive black hole (MBH), (iii) the injection of AGN-driven winds into the resolved scales, and (iv) the spin-induced anisotropy of the overall feedback process. We tested our implementation by following the propagation of the wind-driven outflow into an homogeneous medium, and here we present a comparison of the results against simple analytical models. We also considered an isolated galaxy setup, where the galaxy is thought to be formed from the collapse of a spinning gaseous halo, and there we studied the impact of the AGN feedback on the evolution of the MBH and of the host galaxy. We find that: (i) AGN feedback limits the gas inflow that powers the MBH, with a consequent weak impact on the host galaxy characterized by a suppression of star formation by about a factor of two in the nuclear ( $\lesssim$ kpc) region; (ii) the impact of AGN feedback on the host galaxy and on MBH growth is primarily determined by the AGN luminosity rather than by its angular pattern set by the MBH spin (i.e., more luminous AGNs more efficiently suppress central star formation (SF), clearing wider central cavities and driving outflows with larger semiopening angles); (iii) the imprint of the angular pattern of AGN radiation emission is detected more clearly at high (i.e., Eddington) accretion rates. At such high rates, the more isotropic angular patterns, as occur for high spin values, sweep away gas in the nuclear region more easily, therefore causing a slower MBH mass and spin growths and a higher quenching of SF. We argue that the influence of spin-dependent anisotropy of AGN feedback on MBH and galaxy evolution is likely to be relevant in those scenarios characterized by high and prolonged MBH accretion episodes and by high AGN wind–galaxy coupling. Such conditions are more frequently met in galaxy mergers and/or high-redshift galaxies.

**Key words.** methods: numerical – galaxies: active – galaxies: evolution – quasars: supermassive black holes – galaxies: Seyfert – galaxies: star formation

## 1. Introduction

It is now widely accepted that at the center of each galaxy resides a massive black hole (MBH, Kormendy & Ho 2013). The mechanisms responsible for the very formation of MBHs in the high-redshift Universe are still debated (see, e.g., Volonteri et al. 2021, and references therein), but there is a consensus that most of their mass accumulates over cosmic time through gas accretion (Soltan 1982), accompanied by substantial energy releases observed in emission in luminous active galactic nuclei (AGNs) (Lynden-Bell 1969). Under specific conditions, the energy radiated by AGNs can even surpass the binding energy of the host galaxy (Bower et al. 2012). Consequently, AGN radiation has the potential to exert a significant influence on the host galaxy in the case of effective interaction with the interstellar medium (ISM); this phenomenon is known as AGN feedback. This implies that MBHs are not mere spectators in the galaxy formation process; rather, they play a pivotal role in it.

One of the possible ways in which AGN interact with their host galaxy ISM is through galaxy-wide ( $\geq 0.1$ –10 kpc) energetic outflows and turbulence (e.g., Nesvadba et al. 2011;

Cicone et al. 2018; Veilleux et al. 2020; Fluetsch et al. 2021). Theoretically, these outflows may be driven by radiation pressure or AGN-driven winds and could occur over scales ranging from the accretion disk ( $\leq 10^{-2}$  pc) to galaxy-wide scales, where they could affect the properties of the gas in the ISM and beyond. This interplay between AGN feedback and the galaxy ISM results in AGN feedback regulating both the host galaxy star formation (SF) and the MBH growth (Harrison 2017), suggesting AGN feedback plays a role in the explanation of the tight scaling relations between galaxy properties and the mass of the central MBH (Magorrian et al. 1998; Ferrarese & Merritt 2000; Häring & Rix 2004).

Due to its relevance, AGN feedback has become an imperative ingredient in modern theories of galaxy formation, and is needed to reproduce key observables of galaxy populations; it is therefore routinely incorporated both in semianalytic (Kauffmann & Haehnelt 2000; Croton et al. 2006; Henriques et al. 2015) and hydrodynamical simulation models (Vogelsberger et al. 2014; Hirschmann et al. 2014; Schaye et al. 2015; Davé et al. 2019; Weinberger et al. 2017). Despite this central importance of MBHs, the physical processes governing gas accretion and the associated feedback processes are only poorly understood and the modeling in cosmological hydrody-

\* Corresponding author; [fbollati@studenti.uninsubria.it](mailto:fbollati@studenti.uninsubria.it)

dynamic simulations (where MBH accretion disk scales cannot be properly resolved) is therefore sketchy, and is typically encapsulated in heuristic subgrid models.

Subgrid feedback models in Lagrangian codes (based on particles or moving mesh) typically fall into two categories: thermal and kinetic energy injection modes. In thermal mode, AGN feedback is modeled by injecting an amount of thermal energy into the neighboring gas particles at a rate that is directly proportional to the AGN bolometric luminosity (Springel et al. 2005; Di Matteo et al. 2005; Costa et al. 2014). While some modifications have been introduced, black hole accretion and quasar feedback follow this basic model in most state-of-the-art cosmological simulations (Vogelsberger et al. 2013; Schaye et al. 2015; Tremmel et al. 2017; Weinberger et al. 2017; Henden et al. 2018; Lupi et al. 2019, 2022). On the other hand, in kinetic mode, energy is injected in kinetic form into a number of cell/particle neighbors (e.g., Choi et al. 2012; Barai et al. 2016, and the ‘low accretion mode’ in Weinberger et al. 2017; Anglés-Alcázar et al. 2017a; Davé et al. 2019; Sala et al. 2021). Both these methods have some limitations (see Sect. 5.1 of Costa et al. 2020 for a detailed discussion): (i) they fail to reproduce the correct AGN wind thermalization scale, provided this can be resolved, (ii) they are accompanied by a decrease in the resolution around the accreting black hole once the neighboring gas particles are driven outwards by the energy injection, and (iii) the injection itself is anisotropic as it follows the mass distribution of the neighboring gas particles. Costa et al. (2020) proposed a novel subgrid model in which wind mass is explicitly injected along with momentum and energy at a fixed spatial scale across a desired solid angle, independently of the configuration of the gas cells surrounding the black hole. A similar approach is followed by Torrey et al. (2020), who directly spawn wind particles and eject them outward into the MBH surrounding resolved scales. Both these “wind injection” approaches do not suffer from the limitations mentioned above.

An important parameter to be considered when modeling AGN feedback, and more generally MBH evolution, is the MBH spin, given the complex nonlinear influence spin and feedback have on each other. Indeed, on one hand the spin modulates the radiative efficiency of AGN disks, which influences the MBH accretion and the amount of energy released in radiation, and – for thick radiatively inefficient disks – regulates the kinetic power and direction of jets (Blandford & Znajek 1977). On the other hand, feedback strongly impacts the MBH spin growth as it affects the gas reservoir that fuels MBH accretion, which, together with MBH mergers, is the main channel for spin evolution (Berti & Volonteri 2008). In addition to its relevance in the context of AGN feedback, the spin has a strong influence on the gravitational wave emission of merging BHs (Klein et al. 2016), and thus also on the expected recoil velocity of the merger remnant (Dotti et al. 2010), which make the spin a fundamental parameter to be considered when our aim is to better understand the cosmic evolution of MBHs. Due to its importance, some recent studies included spin evolution in hydrodynamical simulations (Fiacconi et al. 2018; Bustamante & Springel 2019; Cenci et al. 2021; Dubois et al. 2021) and semianalytical models of galaxy formation (Volonteri et al. 2005; Fanidakis et al. 2011; Barausse 2012; Sesana et al. 2014). These studies, together with observations (Reynolds 2021), show that the distribution of MBH spins depends on several quantities, such as host galaxy morphology, MBH mass, and redshift.

Recently, Campitiello et al. (2018) first discussed the influence that the MBH spin has in shaping the angular pattern of the AGN radiation, showing that more rapidly spinning

black holes result in more isotropic radiation patterns, as the geodesics of photons emitted in the inner region of the disk undergo stronger gravitational bending. Ishibashi et al. (2019) and Ishibashi (2020) first explored the relevance of this effect in the context of radiation pressure-driven outflows in isolated spherical galaxies by means of semianalytic models. These authors showed that AGNs with rapidly spinning MBHs launch quasi-spherical outflows propagating on large scales at all inclination angles, as opposed to MBHs with low spin values, which produce weaker bipolar outflows driven in the polar direction. As a consequence, Ishibashi (2020) argued that AGNs with slowly spinning MBHs should be accompanied by higher obscuration levels and higher accretion rates, as the AGN radiation is less prone to removing gas from the equatorial plane of the disk. Numerical simulations also suggest that the AGN anisotropic radiation can have a dramatic effect on the outflow properties (Williamson et al. 2019) and MBH pair dynamics (Bollati et al. 2023), but in these studies the anisotropy factor remains unconstrained and is simply left as a free parameter.

In the present paper, we demonstrate a new implementation of AGN radiative feedback in the code GIZMO (Hopkins 2015) that takes into account the spin dependence of feedback anisotropy. In this model, accretion from resolved scales onto an unresolved (subgrid) AGN disk, spin evolution, the injection of AGN winds into resolved scales, and their spin-induced anisotropy are all self-consistently evolved. This implementation builds upon existing modules for MBH accretion and spin evolution (Cenci et al. 2021) and AGN wind (Torrey et al. 2020). Equipped with this model, we investigated the role of AGN wind anisotropy in shaping AGN-driven outflows and the evolution of isolated disk galaxies hosting active MBHs. This paper is organized as follows: in Sect. 2 we review the spin-dependence of the angular pattern of AGN radiation and we connect it to the anisotropy of AGN winds. The implementation of this effect in GIZMO is presented in Sect. 3, and in Sect. 4 we present some tests of this model. We discuss an application of our new implementation in the context of isolated disk galaxies in Sect. 5, and draw conclusions in Sect. 6.

## 2. Theoretical background

In this section, we review how the MBH spin influences both the accretion-disk radiative efficiency and the angular pattern of the emitted radiation, and we show how this reflects on the properties of AGN radiation-driven winds. Then, we discuss two analytic solutions of outflows driven by such anisotropic winds.

### 2.1. Radiation angular pattern from accretion disks

The MBH spin is characterized by the dimensionless spin parameter  $a = cJ_{\bullet}/GM_{\bullet}^2$ , where  $J_{\bullet}$  is the MBH angular momentum magnitude,  $M_{\bullet}$  the MBH mass,  $c$  the speed of light in vacuum and  $G$  the gravitational constant. The MBH spin determines the location of the innermost stable circular orbit (ISCO) (Bardeen et al. 1972) of accretion disks and hence their radiative efficiency  $\eta$ ; that is, the fraction of rest-mass energy accreting onto the BH  $\dot{M}_{\text{acc}}c^2$  that is converted in luminosity  $L$ :

$$\eta(a) \equiv \frac{L}{\dot{M}_{\text{acc}}c^2}. \quad (1)$$

Indeed, the gas in the disk, in order to reach a smaller ISCO, as occurs for higher spin values, needs to dissipate more energy through viscous torques, which results in higher temperatures and higher radiation output.

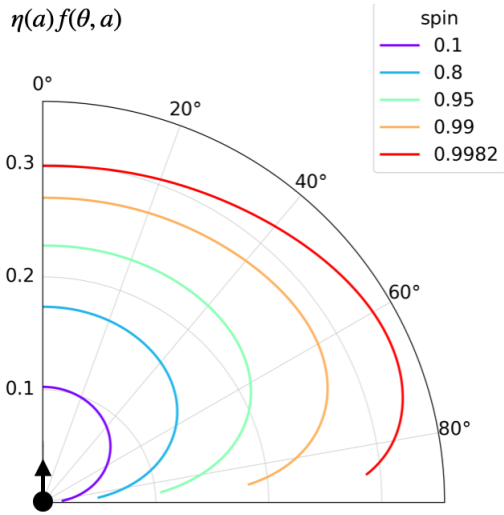


**Fig. 1.** Luminosity angular pattern  $\eta(a)f(\theta, a)$  for different spin values.

Recently, [Campitiello et al. \(2018\)](#) and [Ishibashi \(2020\)](#) pointed out that the BH spin not only influences the amount of energy released in radiation during the accretion process, i.e., the disk luminosity, but also the angular pattern of such radiation. This is a consequence of the spin-dependence of the location of the ISCO and of the relativistic gravitational bending of photons being more effective closer to the BH, i.e., in a stronger gravitational field. Indeed, in the Newtonian case, with straight-lines photon geodesics, the luminosity angular distribution follows a simple cosine-like pattern, with the maximum luminosity observed when the disk is face-on and the minimum in the side-on configuration. If we take into account photon geodesics in full GR, due to the gravitational bending more radiation is capable to reach to observer's eye in the side-on configuration, and this occurs in a way that is sensitive to the BH spin. In particular, for larger BH spin values, the ISCO is located nearer to the BH and therefore the photons emitted by the inner annuli of the disk (the ones that dominate the disk luminosity) experience a stronger gravitational bending, funneling more radiation in the side-on direction, yielding a more isotropic radiation angular pattern.

[Campitiello et al. \(2018\)](#) and [Ishibashi \(2020\)](#) computed the precise emission pattern numerically by means of the KERBB model implemented in XSPEC ([Li et al. 2005](#)). In addition, [Campitiello et al. \(2018\)](#) proposed a normalized fitting function  $f(\theta; a)$  describing the luminosity angular pattern for different viewing angles  $\theta$  and spin parameter  $a$ , so that

$$L(\theta; a) = f(\theta; a)L \quad (2)$$

is the luminosity measured by an observer whose line-of-sight forms an angle  $\theta$  with the spin direction. With the above definition, the optically thick emission from a non-relativistic disk (i.e., when any light bending is neglected) would be described by  $f(\theta, a) = f(\theta) = 2 \cos \theta$ . The term  $f(\theta, a)\eta(a)$ , in the relativistic case, is shown in Fig. 1.

In order to quantify the degree of anisotropy as a function of the BH spin, we define an *effective semiopening angle*  $\theta_{\text{eff}}(a)$ , as the truncation angle of the corresponding isotropic emission such that its angle-integrated output equals that of the actual angle-dependent emission. In Fig. 2 we show  $\theta_{\text{eff}}(a)$  together with  $\eta(a)$ . From this figure we see that we have a smaller  $\theta_{\text{eff}}$ , i.e., a more collimated and anisotropic angular pattern, for low spin values, whereas the radiation distribution is more isotropic (larger  $\theta_{\text{eff}} \approx 90^\circ$ ) for high spin values. Similarly, from Fig. 1

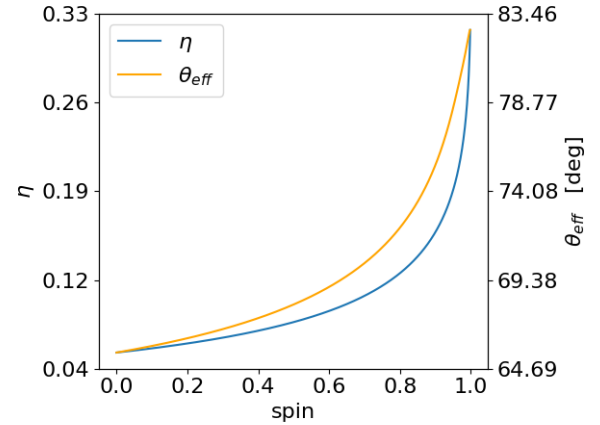


**Fig. 2.** Radiative efficiency (left y-axis) and the effective radiation semiopening angle (right y-axis) as a function of the spin parameter  $a$ .

we see that in spin close to zero, the radiative flux is vertically focused along the spin axis and it decreases with increasing  $\theta$ . On the other hand, the flux reduction for high  $\theta \lesssim 90^\circ$  becomes less pronounced for increasing spin values, i.e., the flux collimation decreases moving towards a nearly isotropic radiation pattern.

## 2.2. AGN feedback

As [Ishibashi et al. \(2019\)](#) and [Ishibashi \(2020\)](#) pointed out, if the radiation from the accretion disk couples to the surrounding material by exerting radiation pressure on dust or by launching line-driven AGN winds, then the emerging outflow inherits the anisotropy of the impinging radiation, which, in turn, it is shaped by the BH spin. This outflow spin-dependent anisotropy can affect the outflow ability to couple with the ISM and hence it may change the impact that AGN feedback has on the host galaxy and on the MBH growth. In this way, the MBH spin, through its influence on AGN feedback, can possibly play a role in the MBH-galaxy host co-evolution.

Galactic AGN driven outflows in the so-called quasar mode are typically described as the result of the interaction between the disk radiation with the surrounding material and with the transfer of energy and momentum to it. Many works assume that this coupling occurs at the scale of the accretion disk and broad line region (BLR), launching an AGN wind that mediates the interaction between the AGN radiation and the ISM ([King 2003](#); [Zubovas & King 2012](#); [Faucher-Giguère & Quataert 2012](#); [Costa et al. 2014, 2020](#); [Hartwig et al. 2018](#); [Torrey et al. 2020](#)). Another possibility is that the radiation escapes the inner region and couples at the ISM scale directly through radiation pressure on dust ([Murray et al. 2005](#); [Ishibashi & Fabian 2015](#); [Thompson et al. 2015](#); [Costa et al. 2018](#); [Barnes et al. 2018](#)). In the following we are going to focus on the first mechanism; that is, AGN-wind-driven outflows.

### 2.2.1. AGN winds

Observations of bright quasars with blueshifted X-ray absorption lines ([Pounds et al. 2003](#); [Reeves et al. 2009](#); [Tombesi et al. 2015](#)) give strong evidence for intense winds from galactic nuclei characterized by relativistic velocities. Such winds are believed to be launched by Thompson scattering or line-driven momentum transfer of AGN radiation to the gas. If each

photon emitted by the AGN interacts just once with the gas, then the transferred momentum flux equals the radiation momentum flux  $L/c$ . If the gas is dusty, then the optical and ultraviolet (UV) radiation is absorbed and re-emitted at infrared (IR) wavelengths. If the gas is optically thick in the IR, instead of streaming out, the reprocessed IR photons undergo multiple scatterings. In this case, the net momentum imparted by the AGN radiation field may exceed  $L/c$ . More generally we indicate with  $\tau L/c$  the momentum transferred to the gas, where the parameter  $\tau$  holds the information concerning the radiation-gas coupling and  $\tau = 1$  ( $> 1$ ) in the single(multi)-scattering scenario. Then, the total momentum carried by the wind can be written as

$$\dot{P}_w = \tau \frac{L}{c}. \quad (3)$$

Using Eq. (2) and by writing the momentum loading as  $\dot{P}_w \equiv \int \dot{p}_w(\theta) r^2 d\Omega$ , where  $\dot{p}_w(\theta)$  is the wind momentum flux in the direction  $\theta$  at a distance  $r$  from the AGN, Eq. (3) yields

$$\dot{p}_w(\theta; a) = \tau \frac{L}{c} \frac{f(\theta; a)}{4\pi r^2}. \quad (4)$$

That is, the momentum flux of the wind follows the same angular pattern of the radiation. Assuming that the wind is launched at a constant velocity  $v_w$ , then the mass flux in the direction  $\theta$  is simply  $\dot{m}_w(\theta; a) = \dot{p}_w(\theta; a)/v_w$ , and hence the mass flux angular distribution of the wind follows the same angular pattern as well. By combining Eqs. (1) and (3) instead we obtain the total mass loading:

$$\dot{M}_w \equiv \frac{\dot{P}_w}{v_w} = \eta_w \dot{M}_{\text{acc}}, \quad (5)$$

where we define the mass loading factor,

$$\eta_w = \eta(a) \tau \frac{c}{v_w}. \quad (6)$$

### 2.2.2. Wind-driven outflows

The further evolution of wind-driven outflows has been discussed in many papers (Weaver et al. 1977; Koo & McKee 1992; King 2003; Costa et al. 2014; Hartwig et al. 2018) and textbooks (Dyson & Williams 1997), in the context of both stellar and AGN feedback. We briefly review some aspects here.

Once launched, the AGN wind moves in the ambient medium shovelling the material it encounters along its path, forming a shell expanding at constant velocity  $\sim v_w$ . This phase is referred to as free-expansion and lasts approximately until the swept-up mass equals the mass of the impinging wind. If the ambient medium has uniform density  $\rho_0$ , the free expansion timescale reads

$$t_{\text{free}} = \left( \frac{3}{4\pi} \right)^{1/2} \left( \frac{\dot{M}_w}{\rho_0 v_w^3} \right)^{1/2}. \quad (7)$$

When the shell radius reaches a distance of  $\sim R_{\text{free}} \equiv v_w t_{\text{free}}$ , the momentum of the material added to the shell start causing it to slow down significantly and free-streaming brakes down. From now on, the incoming wind forms a strong reverse shock against the slowing down shell and a significant fraction of the wind kinetic energy is thermalized. We can now distinguish a four-layers structure formed by the AGN wind, the shocked wind, the shocked ambient medium and finally the unperturbed environment. The dynamics of

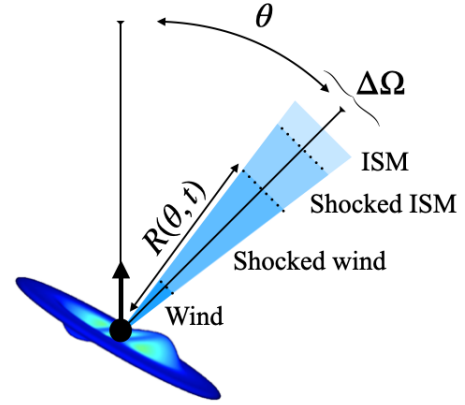


**Fig. 3.** Schematic view of the outflow structure in a slice subtended by a solid angle  $\Delta\Omega$  and centered in a direction forming an angle  $\theta$  with the MBH spin. This stratified structure comprises the AGN wind, the shocked wind (which extends up to a distance  $R(\theta, t)$  from the MBH), the shocked ISM, and the unperturbed ISM. The illustration also shows the warped accretion disc that feeds the spinning MBH.

this structured shell, or outflow, has been studied extensively both theoretically (Weaver et al. 1977; Koo & McKee 1992; Dyson & Williams 1997; Faucher-Giguère & Quataert 2012; Zubovas & King 2012; King & Pounds 2015) and numerically (Costa et al. 2014, 2020). In a nutshell, the subsequent evolution of the outflow depends on the ability of the shocked wind to preserve its thermal energy, which in turn depends on the cooling processes involved and on the associated timescales. If radiative losses in the shocked wind are negligible, it expands adiabatically doing “ $PdV$ ” work on the shocked ambient medium, driving an “energy driven” outflow (King 2005). If the shocked wind is radiatively cooled, the shell of swept-up ambient gas is driven solely by the wind’s ram pressure (King 2003). Such solutions are termed “momentum driven”. If the shocked wind does cool, but inefficiently, the wind solution is intermediate between momentum and energy-driven (Faucher-Giguère & Quataert 2012).

From an observational point of view, both energy and momentum driven outflows have been detected (Fluetsch et al. 2019; Tozzi et al. 2021). However, the observed outflows are mostly on kiloparsec (kpc) scales, while theoretical arguments (Faucher-Giguère & Quataert 2012; King & Pounds 2015) and the lack of observational evidence of cooling wind shocks (Bourne & Nayakshin 2013) suggest that under realistic circumstances the shocked wind bubble cools inefficiently, and that momentum-driven outflows should be confined within the central few 100 pc from the MBH. Therefore, outflows observed in the momentum driven regime are more consistent with a radiation pressure on dusty gas mechanism or with an energy-driven outflow poorly coupled with the ISM, rather than with an efficiently cooling wind-driven outflow.

### 2.2.3. Energy and momentum outflows driven by anisotropic winds

We now describe how we derive the analytic solution for the propagation in a homogeneous medium of an outflow driven by an anisotropic wind, both in the energy- and momentum-driven scenarios. We characterize the evolution of the outflow by calculating the location  $R(\theta, t)$  of the contact discontinuity that separates the shocked wind from the shocked ambient medium (see Fig. 3). In the energy driven regime, the shocked wind shell is hot

and thick and its thermal energy evolution is due to the energy injected by the wind (suddenly converted in thermal energy) and the work done on the above shocked ambient medium. Using Eqs. (1) and (5), we have that the thermal energy is added to the shock wind layer at a rate  $1/2\dot{M}_w v_w^2 = 1/2\tau(v_w/c)L \equiv \epsilon L$ , where  $\epsilon = 1/2\tau v_w/c$ . Now, if we consider a single slice of the outflow, in the direction  $\theta$  and subtended by a solid angle  $\Delta\Omega$ , as in Fig. 3, then the impinging disk luminosity in the slice direction is  $Lf(\theta, a)\Delta\Omega/4\pi$  (see Eq. (2)) and a fraction  $\epsilon$  of it is converted in thermal energy in the shocked wind layer of the slice. Then, if  $P$  is the pressure of the shocked wind layer, the pressure force exerted on the layer above can be written as  $P\Delta\Omega R^2$  and the  $PdV$  work as  $P\Delta\Omega R^2 dR$ . Assuming that the shocked wind layer is thick enough to neglect the portion of the slice occupied by the freely streaming wind, its volume can be approximated with that of the slice up to  $R$ , i.e.  $\Delta\Omega R^3/3$ , and hence its internal energy with  $(3/2)P\Delta\Omega R^3/3$ . Then, if  $\rho_0$  the ambient medium density we can write the conservation of the shocked wind energy and the conservation of the shocked ambient medium momentum of the slice as

$$\frac{d}{dt} \frac{3}{2} \left( \frac{\Delta\Omega}{3} R^3 P \right) = \epsilon L f(\theta; a) \frac{\Delta\Omega}{4\pi} - \Delta\Omega R^2 \dot{R} P, \quad (8)$$

$$\frac{d}{dt} \left( \rho_0 \frac{\Delta\Omega}{3} R^3 \dot{R} \right) = R^2 \Delta\Omega \dot{P}, \quad (9)$$

respectively. By solving Eq. (9) for  $P$  and replacing in Eq. (8) we get

$$10R^2 \dot{R}^3 + 8R^3 \dot{R} \ddot{R} + \frac{2}{3} R^4 \ddot{\dot{R}} = \frac{v_w L f(\theta; a)}{2c\pi\rho_0}, \quad (10)$$

which admits the self-similar solution

$$R_{\text{sh}}(\theta, t) = \left( \frac{125}{308\rho_0\pi} \frac{v_w}{c} L f(\theta; a) \right)^{1/5} t^{3/5}. \quad (11)$$

Equation (11) describes the evolution of the contact discontinuity in time, for each direction  $\theta$ , in the energy driven regime.

In momentum-driven outflows, the energy of the shocked wind is quickly dissipated on small scales via radiation losses and the shocked wind shell collapses into a thin layer, as its thermal pressure support is radiated away. Then, the shocked ambient medium layer is driven outward directly by the ram pressure of the impinging AGN wind, which equals the momentum flux of the disk radiation if  $\tau = 1$ . In this case, we write the momentum conservation of the shocked ambient medium in the slice as

$$\frac{d}{dt} \left( \rho_0 \frac{\Delta\Omega R^3}{3} \dot{R} \right) = \frac{L f(\theta; a) \Delta\Omega}{4\pi c}, \quad (12)$$

which is solved by

$$R_{\text{sh}}(r, \theta, t) = \left( \frac{3L f(\theta; a)}{2\pi c\rho_0} \right)^{1/4} t^{1/2}. \quad (13)$$

Equation (13) represents the evolution of the contact discontinuity in the momentum driven regime. We briefly mention that the main cooling process that could make this regime possible is the Compton cooling of free electrons in the shocked wind shell against the AGN photons, as discussed in King (2003), Faucher-Giguère & Quataert (2012), Hartwig et al. (2018), Richings & Faucher-Giguère (2018), Costa et al. (2020), Torrey et al. (2020). Following Sazonov et al. (2004), if we

assume that the AGN radiation field has a nearly obscuration-independent Compton temperature  $T_{\text{AGN}} = 2 \cdot 10^7$  K, the gas Compton heating/cooling rate for gas with temperatures  $T < 10^9$  K (non relativistic regime) is

$$\Lambda_{\text{Cpt}} = \frac{n_e \sigma_T L}{m_e c^2 \pi r^2} k_B (T - T_{\text{AGN}}), \quad (14)$$

where  $T$  is the gas temperature,  $m_e$  the electron mass,  $\sigma_T$  the Thompson cross-section,  $n_e$  the electron number density (bound + free) and  $r$  the distance of the gas element from the AGN.

### 3. Feedback implementation

In order to investigate the role of anisotropic radiative feedback in more realistic scenarios, we implemented the anisotropic spin-dependent AGN wind discussed above (Sect. 2.2.1) in the code GIZMO (Hopkins 2015). In a nutshell, our implementation is characterized by a subgrid accretion disk whose properties (mass  $M_\alpha$  and angular momentum  $\mathbf{J}_\alpha$ ) evolve due to the accretion  $\dot{M}_{\text{in}}$  from resolved scales on the subgrid disk (modeled with a modified Bondi-Hoyle prescription similar to Tremmel et al. 2017) and due to the accretion  $\dot{M}_{\text{acc}}$  within the subgrid disk on the MBH. Similarly, the physical (subgrid) MBH is characterized by its mass  $M_\bullet$  and its angular momentum  $\mathbf{J}_\bullet$  and they evolve according to the subgrid accretion. This model, based on Cenci et al. (2021) and Sala et al. (2021) (see also Fiacconi et al. 2018), tracks the exchange of angular momentum between the MBH and the subgrid disk due to both the accretion on the MBH and the Bardeen-Petterson torque (Bardeen & Petterson 1975), in this way following the MBH spin evolution consistently with evolution of the subgrid disk properties. More details about the accretion and spin evolution models are provided in Appendix A.

In the following we present our AGN feedback model, based on the wind-spawning technique<sup>1</sup> developed by Torrey et al. (2020), whose approach is similar to that devised by Costa et al. (2020) for AREPO. Contrary to the AGN feedback models based on thermal/kinetic energy injection in the gas particles neighboring the MBH, Torrey et al. (2020) and Costa et al. (2020) directly inject the wind mass, momentum, and energy from a subgrid region into the resolved scales and let the thermalisation of the wind arise naturally from the hydrodynamic evolution. While in these models the wind injection is assumed isotropic, here we force the wind momentum (Eq. (4)) and mass fluxes to follow the subgrid disk luminosity angular pattern resulting from gravitational bending, which is ultimately set by the MBH spin. We mention that another source of AGN feedback anisotropy does exist when AGN winds are accelerated at relativistic velocities. Indeed, an isotropic AGN radiation source driving a nuclear wind with relativistic velocity is perceived as anisotropic by the wind gas itself due to relativistic beaming (Luminari et al. 2020). However, this effect translates into angular variations of  $v_w$  of a few percent for  $v_w = 0.01c$ , as we assume below, which is negligible compared to the variation in the wind momentum attributed to the photons gravitational bending.

Overall, the MBH mass and spin are evolved in a subgrid fashion according to the properties of the subgrid accretion disk, which are influenced by the resolved accretion flow on the subgrid system. The presence and characteristics of such an inflow

<sup>1</sup> For the sake of completeness, we mention that the spawning particle technique has also been used with the GIZMO code in the context of stellar feedback (Grudić et al. 2021), AGN jets (Su et al. 2021), and AGN winds in zoom-in simulations (Mercedes-Feliz et al. 2023).

**Table 1.** Parameters of test simulations.

	$a$	$\eta$	$\log(M_{\bullet}/M_{\odot})$	$f_{\text{Edd}}$	$L$ [erg/s]	$\mu n$ [cm $^{-3}$ ]	$\epsilon_{\text{grav}}$ [pc]	$N_{\text{w}}$
Energy driven	0.01	0.057	7	0.1	$1.2 \cdot 10^{44}$	1	0.11	588
	0.95	0.190	7	0.332	$3.98 \cdot 10^{44}$	1	0.11	588
	0.9982	0.323	7	0.567	$6.8 \cdot 10^{44}$	1	0.11	588
Momentum driven	0.01	0.057	10	0.3	$3.6 \cdot 10^{47}$	$10^6$	0.08	108
	0.95	0.190	10	0.997	$1.2 \cdot 10^{48}$	$10^6$	0.08	108
	0.9982	0.323	10	1.7	$2.04 \cdot 10^{48}$	$10^6$	0.08	108

**Notes.** Summary of the parameters adopted in our simulations: in order, we show the spin, the radiative efficiency, the MBH mass, the dimensionless accretion rate, the AGN luminosity, the gas number density, the gravitational softening, and the number of particles spawned at each spawning episode. In all simulations, we employed  $10^7$  gas particles, and the velocity and temperature of wind particles were initialized with  $v_{\text{w}} = 0.01c$  and  $T_{\text{w}} = 2 \cdot 10^4$  K.

are affected by the feedback magnitude and anisotropy, which in turn are set by the subgrid disk and MBH properties. This results in a complex nonlinear interplay between MBH fueling, feedback, its anisotropy and the MBH spin, which our subgrid model is aimed to capture. In the following we provide more details about the wind launching implementation.

Following Torrey et al. (2020) and Costa et al. (2020), we assume that a factor  $\tau$  of the radiation momentum flux is transferred to the gas at subgrid scales, generating an AGN wind which is directly injected into the resolved scales. The wind mass outflow rate  $\dot{M}_{\text{w}}$  is computed from the unresolved disk accretion rate as shown in Eq. (5), where both  $v_{\text{w}}$  and  $\tau$ , appearing in the definition of  $\eta_{\text{w}}$  (Eq. (6)), are free parameters of the model. In practice, the wind is simulated by removing mass from the subgrid disk and by spawning  $N_{\text{w}}$  new gas particles at a rate  $\dot{M}_{\text{w}}$ . The newborn wind particles are distributed uniformly on a sphere centered on the MBH and with radius equal to the minimum between one tenth of the MBH gravitational softening  $\epsilon_{\bullet}$  and half of the smallest MBH-gas particle separation. The mass distribution of the spawned particles follows the subgrid disk luminosity angular pattern. More precisely, the mass of the  $i$ -th spawned particle, with polar angle  $\theta_i$  from the MBH spin direction, is assigned as

$$m_i = \frac{f(\theta_i, a)}{\sum_j f(\theta_j, a)} M_{\text{spawn}}, \quad (15)$$

where the sum at denominator spans over all the spawned particles,  $M_{\text{spawn}}$  is the total mass to be spawned and  $f(\theta, a)$  is the luminosity angular pattern defined in Eq. (2).

The wind particles are then launched radially outward with constant velocity  $v_{\text{w}}$  and by interacting with the other surrounding gas particles they generate an outflow. During their evolution, the wind particles can be merged into nonwind (or ISM) gas particles, properly transferring to them their mass, momentum, and energy as in an inelastic collision; see Appendix E of Hopkins (2015). We required that such a merger occurs once the velocity of the target wind particle falls below five times the mean velocity of the nonwind particles in its kernel. We provide more details about wind particles mass resolution and their merger to nonwind particles in Appendix C. In order to track the propagation of the wind into the environment, we introduced a scalar wind tracer  $\zeta$ , similarly to Costa et al. (2020), that represents the wind mass fraction of a gas particle. Therefore  $\zeta = 1$  for wind particles, nonwind particles are initialized with  $\zeta = 0$  and  $0 < \zeta < 1$  values characterize nonwind particles that experienced mergers with wind particles.

In order to be able to capture the formation of a momentum-driven outflow our model includes gas Compton cooling. We

assume that the AGN photons interact with the surrounding gas at subgrid scale, launching the AGN wind, and then they are remitted isotropically. Then, such reprocessed photons can scatter with the high-energy electrons of the shocked wind layer of the outflow, making it lose energy and cool. In practice, following (Hopkins et al. 2016), a contribution  $\Lambda_{\text{Cpt}}$  as in Eq. (14) is included when computing radiative cooling or heating of gas particles, where  $r$  is now the distance between the gas particle and the MBH and  $L$  is the instantaneous subgrid disk luminosity computed from Eq. (1).

In the subgrid model described in the present section, the MBH time step  $dt_{\bullet}$  is taken to be small enough to resolve the subgrid accretion, wind launching and spin evolution and large enough to guarantee that the disk attains a steady-state warped profile, as assumed in our prescriptions (Cenci et al. 2021).

## 4. Tests

In order to compare the simulated evolution of the wind-driven outflows against the analytical predictions given by Eqs. (11, 13), we first adopt an idealized setup. We consider an active MBH embedded in a gas with uniform density and temperature, so to ensure that the outflow anisotropy is the result of the intrinsic anisotropy of the wind, rather than of the ambient density distribution. In order to compare the simulated outflows with Eqs. (11, 13), we switch off gravitational forces and gas self-gravity so that the outflow evolution is purely hydrodynamical. For the entire duration of the simulations, we keep the AGN luminosity and angular pattern constant; that is, we force the properties of the subgrid disk and MBH to remain constant.

In order to test both energy- and momentum-driven outflows, we consider two different setups. In the first case, we assume a gas number density  $\mu n = 1 \text{ cm}^{-3}$ , where  $\mu$  is the mean-molecular-weight, and a MBH mass  $10^7 M_{\odot}$ , while in the second  $\mu n = 10^6 \text{ cm}^{-3}$  and MBH mass  $10^{10} M_{\odot}$ . In both cases the gas temperature is set at  $T = 2 \cdot 10^4$  K. In order to test different outflow anisotropies, for each setup we consider three different values of the MBH spin,  $a_{\bullet} = \{0.01, 0.95, 0.9982\}$ . In the energy-driven simulation with  $a_{\bullet} = 0.01$ , we assume  $f_{\text{Edd}} \equiv \dot{M}_{\text{acc}}/\dot{M}_{\text{Edd}} = 0.1$  (where  $\dot{M}_{\text{Edd}}$  is the Eddington accretion rate), while  $f_{\text{Edd}} = 0.3$  in the corresponding momentum-driven simulation. In the simulations with higher MBH spin, we keep the same subgrid disk properties as for  $a_{\bullet} = 0.01$ , and therefore the corresponding  $f_{\text{Edd}}$  values scale as  $\eta(a_{\bullet})/\eta(a_{\bullet} = 0.01)$ , according to Eq. (A.6). Energy-driven simulations run up to  $t_{\text{end}} \sim 0.22$  Myr, while momentum-driven ones for  $t_{\text{end}} \sim 1.5$  Myr. The values of the main parameters of all runs are summarized in Table 1.

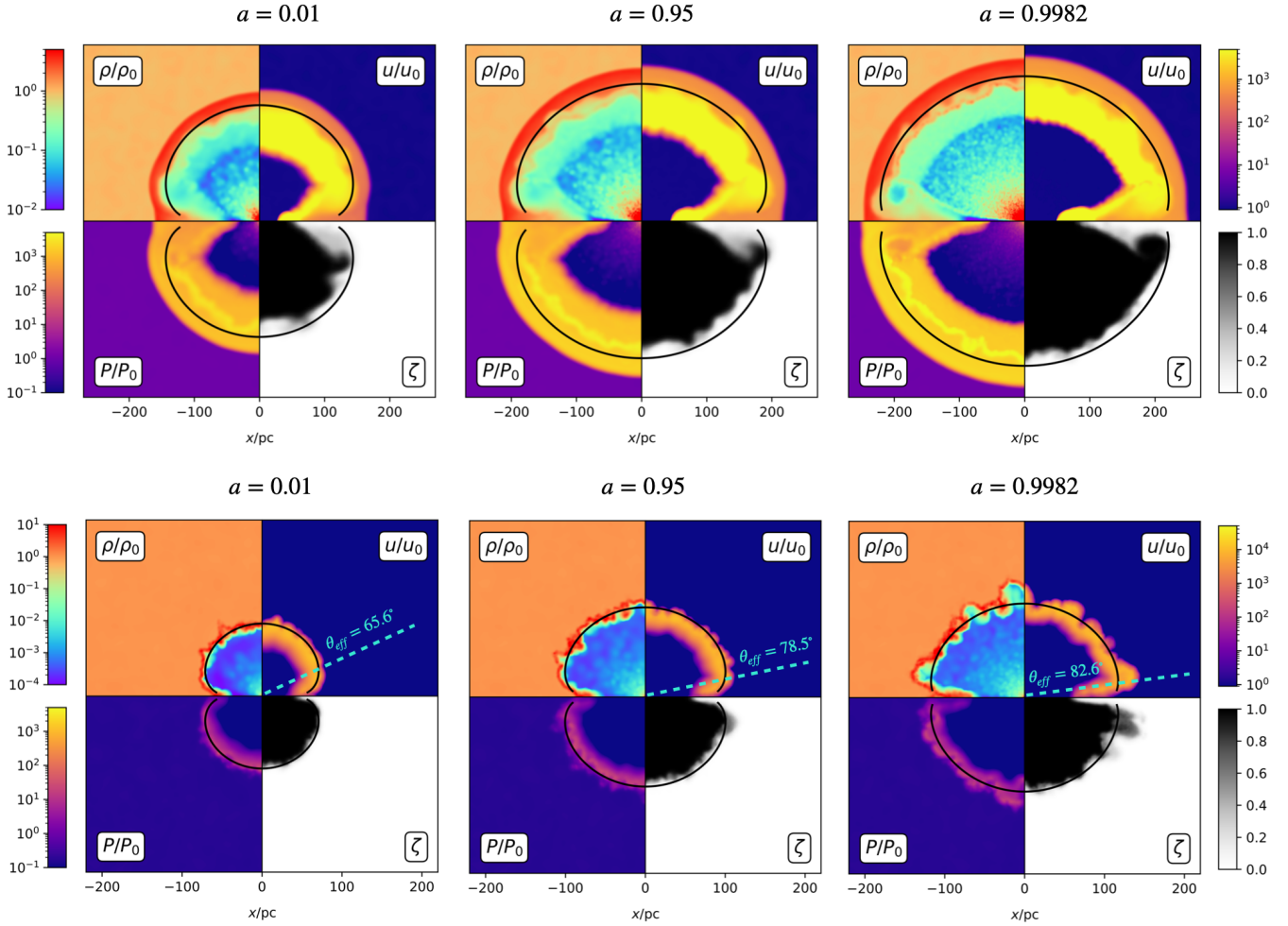


**Fig. 4.** Final snapshots of the propagation of an AGN wind-driven outflow for different spin values (increasing from left to right) and the two considered regimes (energy-driven in the top row and momentum-driven in the bottom one). Each panel illustrates the density, temperature, and pressure fields in units of the corresponding quantities of the assumed background medium as well as the wind mass fraction. In the energy-driven simulations, the outflow can be divided into four distinct sections: (1) the freely expanding wind, (2) the shocked wind, (3) the shocked ambient medium, and (4) the undisturbed ambient medium. In the momentum-driven simulations, radiative cooling makes the shocked wind layer cool and regions (2) and (3) are condensed into a thin shell. The wind tracer is injected together with the wind and is therefore only present in regions (1) and (2). The black lines correspond to the analytical location of the contact discontinuity between regions (2) and (3), as computed in Eqs. (11)–(13). In momentum-driven simulations, the cyan dashed lines indicate the effective aperture of the radiation as defined in Sect. 2.1.

Figure 4 shows the final snapshots for all six simulations, with energy-driven runs in the top panels and momentum-driven in the bottom ones. For each snapshot, the figure reports the density, temperature and pressure fields in units of the corresponding quantities of the background medium as well as the wind mass fraction. Superimposed to all maps, we draw as a black curve the location  $R_{\text{sh}}(t_{\text{end}}, \theta)$  of the contact discontinuity, as computed via Eqs. (11, 13). In the energy-driven simulations (top panels) the typical stratified structure of outflows can be recognized, with the free propagation wind layer, the shock wind, the shocked ambient medium and the unperturbed ambient medium. The simulated location of the contact discontinuity approximates very well its theoretical prediction (Eq. (11)). In the momentum-driven simulations (bottom panels) Compton cooling makes the shocked wind layer cool and collapse, forming a thin shell that separates the free expanding wind from the unperturbed medium. Again, the location of the separating shell is in good agreement with the theoretical estimate (Eq. (13)).

In both energy- and momentum-driven simulations, as the spin increases, the angular pattern of the emerging outflow becomes more spherical and spreads at larger distance from the

MBH. This is expected, as larger spin values yield more isotropic luminosity angular patterns as well as more luminous disks.

## 5. Isolated galaxy simulations

We employ now the subgrid model for spin-dependent AGN winds described in Sect. 3 to study the role of wind anisotropy in shaping AGN-driven galactic outflows, and then the impact such outflows have on the host galaxy. We start by constructing an isolated galaxy setup similarly to Costa et al. (2020). We first initialize a gaseous halo of mass  $M_g = f_g M_{200}$ , where  $M_{200} = 10^{12} M_{\odot}$  is the halo (dark matter + gas) virial mass and  $f_g = 0.17$  the gas mass fraction, with a Navarro–Frenk–White (NFW; Navarro et al. 1997) density profile. A  $M_{\bullet} = 10^8 M_{\odot}$  MBH is placed at the center of the system and the gas internal energy is set to guarantee hydrostatic equilibrium in the absence of cooling. The pressure profile has been computed numerically from the gas density and total potential profiles. The halo concentration parameter is  $C = 7.2$ , which gives a halo scale radius  $a_{\text{halo}} = 28.54 \text{ kpc}$  and a virial radius  $r_{200} = C a_{\text{halo}} = 205.5 \text{ kpc}$ .

The gas initial specific angular momentum follows a profile  $j(r, \theta)$ , where  $r$  and  $\theta$  are the spherical radial and polar coordinates, as in Eqs. (12)–(15) of [Liao et al. \(2017\)](#). Such profile is characterized by the halo spin parameter  $\lambda_{\text{sim}}$ , introduced by [Bullock et al. \(2001\)](#) (their Eq. (5)), which is set to  $\lambda_{\text{sim}} = 0.035$ .

Radiative cooling is modelled as described in [\(Hopkins et al. 2018\)](#), assuming initial metallicity  $0.1 Z_{\odot}$  and ignoring radiative cooling processes below  $T < 10^4$  K. Due to the loss of pressure support following radiative cooling, at  $t = 0$  the spinning gaseous halo starts to collapse towards the center and the inner region settles into a galactic disk continuously fed by the outermost falling layers. We emphasize that this initial gas inflow and the subsequent galaxy formation and star formation history are sensitive to the initial halo density profile. In particular, a NFW profile, as assumed here, is likely to enhance these processes compared to other shallower profiles; see for example [\(Miller & Bregman 2013, 2015\)](#).

The gaseous halo is sampled with  $N = 3 \cdot 10^5$  particles only up to a radius of  $0.6 r_{200}$ . We note that the presence of a sharp pressure gradient at  $0.6 r_{200}$  causes an artificial outflow. Nonetheless, this occurs on spatial scales far away from those considered in our analysis, which focus on the central  $\sim 10$  kpc region. In addition, the radius of  $0.6 r_{200}$  within which we sample the gas is tailored to ensure that over the simulated time the boundary effects of this sampling cannot propagate within the central region of interest, as gas particles above  $0.6 r_{200}$  take more than  $\sim 0.7$  Gyr to fall within  $\sim 5$  kpc from the center of the system. The mass resolution of our simulations is  $m_{\text{gas}} = 3.44 \cdot 10^5 M_{\odot}$ . Dark matter is not sampled and enters the simulation as a static analytic potential.

Star formation is treated following [Springel & Hernquist \(2003\)](#), where the effects of unresolved physical processes operating within the interstellar medium (ISM) are captured by an effective equation of state that is applied to all gas with hydrogen number density  $n_{\text{H}} > n_{\text{th}}$ . This effective equation of state is stiffer than that of isothermal gas, because it accounts for additional pressure provided by supernova explosions within the ISM. Stellar particles are spawned stochastically from gas with  $n_{\text{H}} > n_{\text{th}}$  at a rate

$$\frac{d\rho_{\star}}{dt} = (1 - \beta) \frac{\rho_{\text{c}}}{t_{\star}}, \quad (16)$$

where  $\beta = 0.1$  is the mass fraction of massive stars assumed to instantly explode as supernovae,  $\rho_{\text{c}}$  is the density of cold clouds (see [Springel & Hernquist 2003](#), for details) and  $t_{\star} = t_{\star,0} (n_{\text{H}}/n_{\text{th}})^{-1/2}$  is the star formation timescale, with  $t_{\star,0} = 1.5$  Gyr and  $n_{\text{th}} = 0.5 \text{ cm}^{-3}$ . Supernova-driven winds are not modelled, as they would add a further layer of complexity affecting both star formation, the MBH growth and hence AGN feedback (see, e.g., [Dubois et al. 2015](#)). Therefore, our simulations should be regarded as idealized experiments aimed at illustrating how AGN wind modeling affects the impact of MBH feedback on the host galaxy and on the MBH evolution, without “contamination” from supernova-driven winds.

After the first 150 Myr, once a galactic disk has formed and star formation has already reached its peak, MBH accretion and feedback are “switched on”. At this instant, which we denote with  $t_0$ , the gas and stellar mass of the galaxy are, respectively,  $\sim 8.2 \cdot 10^9 M_{\odot}$  and  $\sim 7.5 \cdot 10^9 M_{\odot}$ . Then, we perform six different simulations divided in two sets (labelled with **C** and **E**) corresponding to different MBH accretion prescriptions, each set consisting of three different simulations characterized by different feedback anisotropies (indicated with labels **f**, **iso**, **a0**). In the simulation set labelled with **C**, the sub-

grid accretion disk is forced to maintain the same properties for the entire duration of the simulations, i.e., the disk mass and angular momentum do not change because of accretion onto the MBH and wind ejection. In these simulations, the Eddington factor  $f_{\text{Edd}} \equiv \dot{M}_{\text{acc}}/\dot{M}_{\text{Edd}}$  is kept constant equal to 1 (similarly to [Torrey et al. 2020](#); [Costa et al. 2020](#) and [Mercedes-Feliz et al. 2023](#)), corresponding to a subgrid disk of constant luminosity  $L = 1.2 \cdot 10^{46}$  erg/s. On the contrary, in **E** simulations,  $f_{\text{Edd}}$  is allowed to evolve and its value is set by the instantaneous MBH + subgrid disk properties (Eq. (A.6)), which, in turn, are determined by the inflow on the disk, the accretion on the MBH and wind ejection (see Eqs. (A.1)–(A.4)). In this way, **E**-simulations are able to capture the mutual nonlinear influence that inflows and outflows have on each other and that lead to self-regulated MBH growth<sup>2</sup>. In addition to these simulation sets, we prolonged the simulation for the spinning halo collapse beyond 150 Myr without switching on the AGN, so that the sets **C** and **E** can be compared to the case in which the MBH is not active. We indicate this simulation with **NoFb**.

Both **C** and **E** sets consist of three simulations, accounting for a different wind anisotropy. Simulations **f** have an angular pattern  $f(\theta; a)$ , as illustrated in Sect. 2.1; this pattern evolves according to the evolution of the spin parameter  $a$ ; **iso**-simulations are characterized by an isotropic angular pattern, i.e.  $f = 1$ ; **a0**-simulations assume instead a fixed angular pattern corresponding to the one of  $a \simeq 0$ ,  $f = f(\theta; 0.01)$ . We note that, independent of the anisotropy pattern, the MBH spin and  $\eta(a)$  are allowed to evolve in these runs. The motivation for these choices of angular patterns is the following: real outflows anisotropy can result from the wind “intrinsic” anisotropy imparted by the radiation angular pattern and linked to the MBH spin, i.e. the anisotropy discussed in Sect. 2.1 and seen in Fig. 4, or it can be induced by the anisotropy of the medium in which the outflow propagates as, for example, in a spiral galaxy where the gas density is higher in the midplane of the galaxy than perpendicular to it. In this way, an “intrinsically” spherical outflow expands more easily along the galaxy axis, i.e., along the least resistance path, turning into a bipolar (anisotropic) outflow ([Hartwig et al. 2018](#); [Costa et al. 2020](#); [Zubovas & Maskeliūnas 2023](#))<sup>3</sup>. Since outflow anisotropy is shaped by these two factors, both present in simulations **f**, a comparison with simulations **iso** allows to disentangle these effects and to properly assess the relevance of radiation pattern anisotropy in galactic outflows. Instead, simulations **a0** represent the opposite term of comparison, in which the angular pattern is maximally anisotropic, i.e.  $f(\theta; 0.01) \simeq 2 \cos \theta$  as in (Newtonian)  $\alpha$ -disks, as if all the isotropy coming from gravitational bending were removed. We summarize the main features of the six simulations performed in Table 2.

In both **C** and **E** sets, we start the simulations at  $t_0$  with  $f_{\text{Edd}} = 1$ ,  $a = 0.01$ ,  $M_{\alpha} = 0.005 M_{\bullet}$  and  $M_{\bullet} + M_{\alpha} = 10^8 M_{\odot}$ . The wind velocity and temperature are fixed to  $v_{\text{w}} = 0.01 c$  and  $T_{\text{w}} = 2 \cdot 10^4$ .  $N_{\text{w}} = 48$  wind particles are spawned at each spawning event and the radiation-wind coupling parameter is fixed to  $\tau = 1$ . In all simulations the gravitational softening for all particle species is 2 pc.

In the following subsections, we discuss the impact of AGN feedback in our setups, focusing on the one hand on its effect on the host galaxy, in particular on the central gas

<sup>2</sup> [Torrey et al. \(2020\)](#) showed that an Eddington accreting AGN generates wide cavities in its surroundings, but noted that this lower density should reflect in decreased inflow on the AGN in turn reducing its power and the cavity size itself, letting the system self-regulate.

<sup>3</sup> This may explain, for example, the presence of the Fermi bubbles in the Milky Way ([Zubovas & Nayakshin 2012](#)).

**Table 2.** Isolated galaxy simulations suite.

	$f_{\text{Edd}}(t)$	$M_{\alpha}(t)$
<b>E</b>	Variable	Variable
<b>C</b>	1	$4.975 \cdot 10^5 M_{\odot}$
	Angular pattern	
<b>f</b>	$f(a(t); \theta)$	
<b>a0</b>	$f(a = 0.01; \theta)$	
<b>iso</b>	1	

**Notes.** Main features of the isolated galaxy simulations. (left) The dimensionless accretion rate and subgrid disk mass for the **E** and **C** simulation sets. We note that while subgrid disk quantities are evolved only in **E** simulations, the MBH mass and spin evolve according to the prescriptions detailed in Appendix A in both simulation sets. (right) The AGN radiation angular patterns used in each simulation set.

reservoir and star formation, and on the other hand on its influence on the MBH evolution in mass and spin. Before entering into detail, we provide a qualitative glimpse of how the galaxy–MBH evolution appears in simulations **C\_f** and **E\_f**.

Figure 5 shows three snapshots of the simulation **C\_f**, both face on (top panels) and side-on (bottom panels). In the side-on view, we see that after  $t \simeq 8$  Myr from the AGN “switch on”, a collimated wind is piercing the circumgalactic medium (CGM), its opening angle widening over time. Correspondingly, in the face-on view, a  $\sim$ kpc-scale cavity is cleared in the central region surrounding the MBH, becoming increasingly large with time. Both these effects are accompanied by an increase of the spin value, which reaches  $\sim 0.998$  after  $\simeq 64$  Myr, and hence by an increase in the disk radiative efficiency and in the isotropy of the radiation angular pattern (see discussion in Sect. 2.1). We remark that in this simulation the accretion rate on the MBH is forced to be constant, equal to the Eddington rate. However, as noted by Torrey et al. (2020), once the gas reservoir feeding the MBH diminishes with the formation of a central cavity, the accretion on the MBH should decrease as well, reducing the AGN power and hence its ability to further enlarge the cavity. We show this effect in Fig. 6, which is the analogous of Fig. 5 for the simulation **E\_f**, in which the MBH accretion is consistently evolved with the inflow on the disk and the wind ejection from it. In this case, no cavity formation can be seen in the face-on view and a milder wind (compared to Fig. 5) is seen in the side-on view. This suggests that a much lower accretion (and hence outflow) rate is achieved once that the disk is allowed to adjust itself through its interaction with the environment. In particular, we see in Sect. 5.1.1 that, in this simulation,  $f_{\text{Edd}}$  indeed drops by between one and two orders of magnitude from its initial value.

In Figure 7 we show a zoom-out of the side-on view of simulation **E\_f** at  $t = 24$  Myr. The four columns illustrate, from left to right, the gas density, the wind mass fraction, the gas internal energy, and the electron abundance fraction  $n_e/n_H$ . Even though the AGN wind does not seem to affect much the host galaxy (Fig. 6), it propagates deeply in the CGM creating a hot, low-density, ionized bipolar outflow that extends in the polar directions and regulates the inflow onto the galaxy, hence its growth.

We now discuss more quantitatively the impact of feedback both on the MBH and the galaxy host, turning our attention to the relevance of the spin-dependent wind anisotropy.

### 5.1. The impact of AGN feedback on the MBH

In order to understand how the MBH mass and spin evolve and to what extent their growth is influenced by AGN feedback, we need to understand its back-reaction on  $f_{\text{Edd}}$ , which characterizes the rate of such growth.

#### 5.1.1. Evolution of $f_{\text{Edd}}$

In **C** simulations, the growth of MBH mass and spin is completely determined by the constrain  $f_{\text{Edd}} = 1$ , so it is independent on any effect feedback might have on the gas surrounding the MBH. Conversely, in **E** simulations,  $f_{\text{Edd}}$  varies with time according to the evolution of the subgrid disk+MBH system (Eq. (A.6)), which is influenced by the action of feedback on the nuclear environment. Indeed, in this case, AGN feedback diminishes the gas density in the vicinity of the MBH, lowering the mass inflow rate on it and hence the AGN power.

In order to have a better understanding of how  $f_{\text{Edd}}$  evolves, we compute the time derivative  $df_{\text{Edd}}/dt$  (see Appendix A.2), finding that it can be approximated as

$$\frac{df_{\text{Edd}}}{dt} \simeq 5f_{\text{Edd}} \left( -C_w \frac{\dot{M}_w}{M_{\alpha}} + C_{\text{in}} \frac{\dot{M}_{\text{in}}}{M_{\alpha}} \right), \quad (17)$$

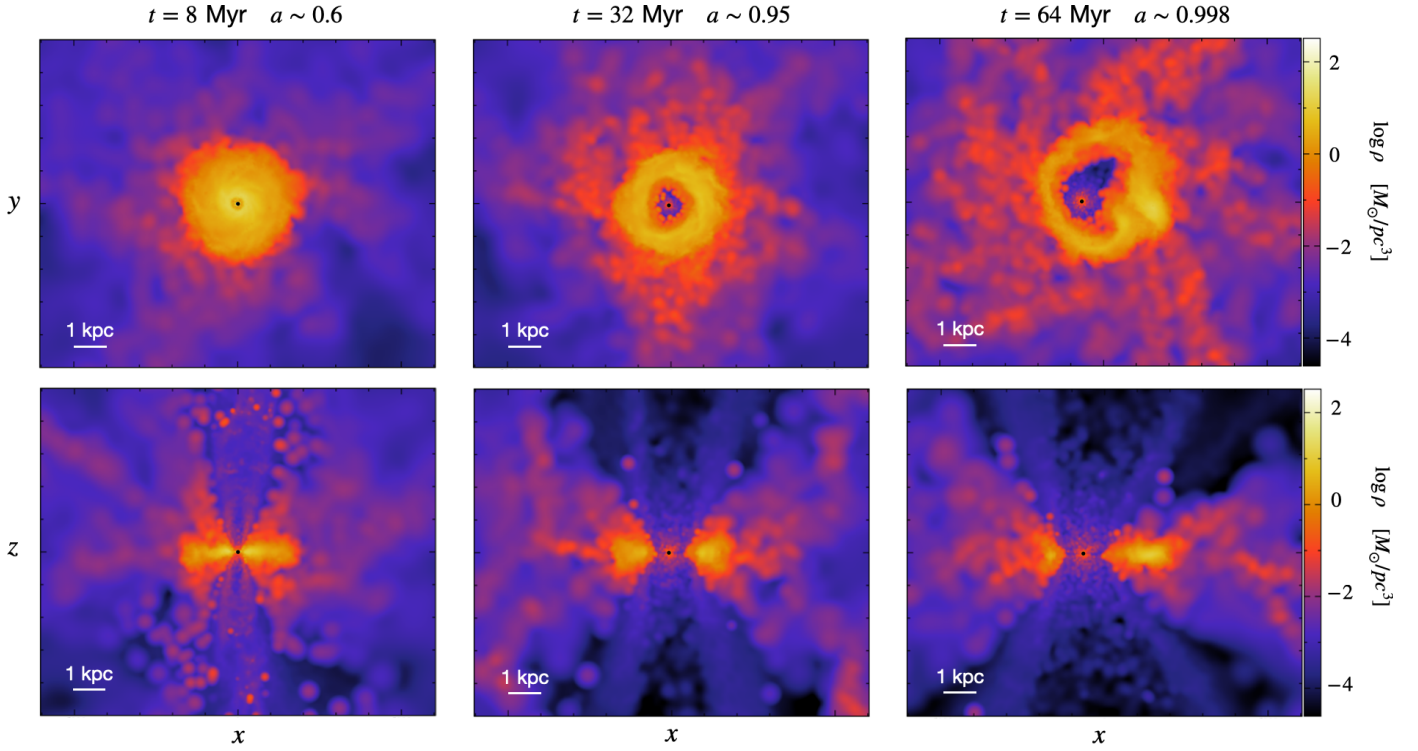
where  $\dot{M}_{\text{in}}$  is the mass inflow rate on the subgrid disk from resolved scales, as defined in Appendix A.1, and the coefficients  $C_w$  and  $C_{\text{in}}$  are both found to be  $\simeq 0.1$ , as detailed in Appendix A.2. Equation (17) describes the evolution of  $f_{\text{Edd}}$  as driven by the disk mass loss, proportional to  $\dot{M}_w$ , and by the inflow  $\dot{M}_{\text{in}}$  that supplies mass to the disk; in other words, the disk accretion rate is regulated by the balance between outflows and inflows. Because of the different signs in front of  $C_w$  and  $C_{\text{in}}$ , the disk tends to evolve towards a stationary  $df_{\text{Edd}}/dt \sim 0$  regime. Indeed, if the inflow exceeds the outflow, i.e.  $C_{\text{in}}\dot{M}_{\text{in}} > C_w\dot{M}_w$ , then the accretion rate  $f_{\text{Edd}}$  increases and  $\dot{M}_w$  grows as well (see Eq. (5)). By contrast, if the disk mass consumption outpaces the external mass supply,  $C_w\dot{M}_w > C_{\text{in}}\dot{M}_{\text{in}}$ , the accretion rate decreases and hence  $\dot{M}_w$  diminishes too. In this way inflows and outflows tend to adjust each other such that  $C_w\dot{M}_w \sim C_{\text{in}}\dot{M}_{\text{in}}$ , i.e.  $df_{\text{Edd}}/dt \sim 0$ .

Figure 8 shows the evolution of  $\dot{M}_w$  and  $\dot{M}_{\text{in}}$  in the three simulations **E** and reveals that in all cases  $\dot{M}_w \sim \dot{M}_{\text{in}}$  and both quantities settle around  $\sim 1 M_{\odot}/\text{yr}$  after a transient of  $\sim 50$  Myr. As a result, in all **E** simulations,  $f_{\text{Edd}}$  decreases from its initial value  $f_{\text{Edd},0} = 1$  and, after  $\sim 50$  Myr, attains a value  $\sim 0.05$  (see Fig. 9), which is consistent with observed Seyfert galaxies (Ho 2009) and corresponds to a moderate luminous AGN with  $L \simeq 6 \cdot 10^{44}$  erg/s.

#### 5.1.2. MBH mass and spin growth

The mass and spin evolution of the MBH in all our simulations is shown in Figure 10. In **C** simulations, the growth of MBH mass and spin is constrained by  $f_{\text{Edd}} = 1$ , whereas in **E** simulations  $f_{\text{Edd}}$  varies with time (Fig. 9), according to the interplay between inflows and outflows, as discussed in 5.1.1. In this second case  $f_{\text{Edd}}$  lowers down to  $\sim 0.05$ , in this way the MBH mass and spin growth is severely delayed compared to the  $f_{\text{Edd}} = 1$  case.

While the disk luminosity is directly linked to the MBH mass and spin growth rates (Eq. (1)), its angular pattern has a negligible impact on them. Nonetheless, in **E** simulations we notice a small dependence of these growth rates with the radiation angular pattern, i.e. the more isotropic the angular pattern is (where isotropy rises with **a0**  $\rightarrow$  **f**  $\rightarrow$  **iso**), the slower the



**Fig. 5.** Density slices of three snapshots from simulation **C\_f**, with the disk face-on in the top panels and side-on in the bottom panels. The MBH location is marked by a black dot.

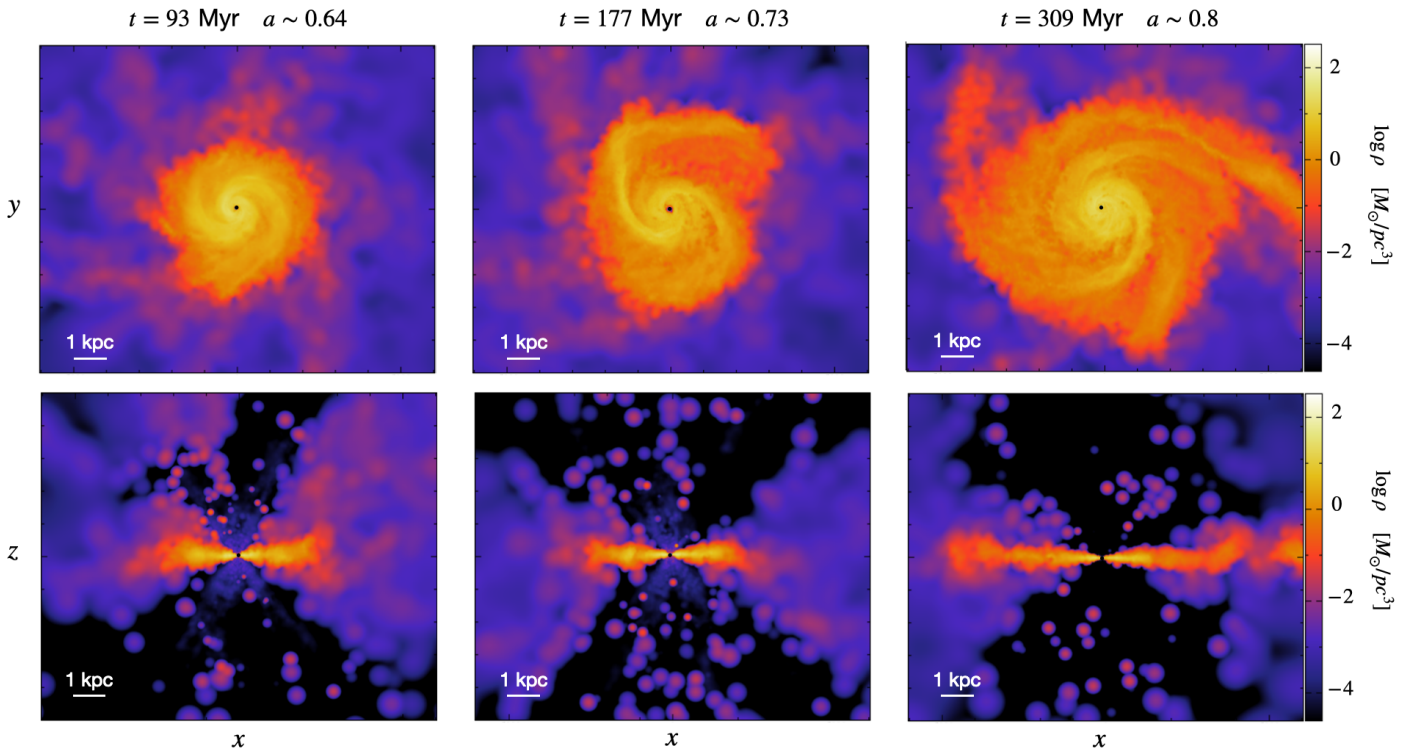


**Fig. 6.** Density slices of three snapshots from simulation **E\_f**, with the disk face-on in the top panels and side-on in the bottom panels. The MBH location is marked by a black dot.

mass and spin growth is. This can be attributed to the wind-ISM coupling increasing with isotropy (see Sect. 5.2), thus yielding smaller mass inflow rates on the MBH and hence lower AGN power.

### 5.2. The impact of AGN feedback on the galaxy host

We now quantify the impact of AGN feedback on the host galaxy by probing the galaxy star formation history, the size of the

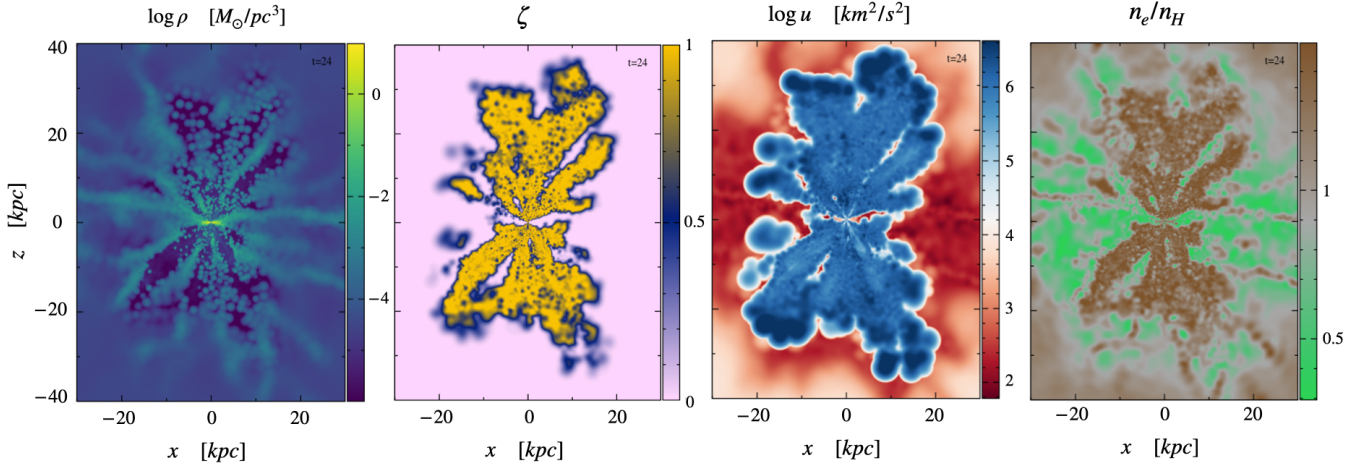


**Fig. 7.** From left to right, edge-on maps of the gas density, the wind mass fraction, the internal energy, and the electron abundance fraction of simulation **E\_f** at  $t = 24$  Myr.

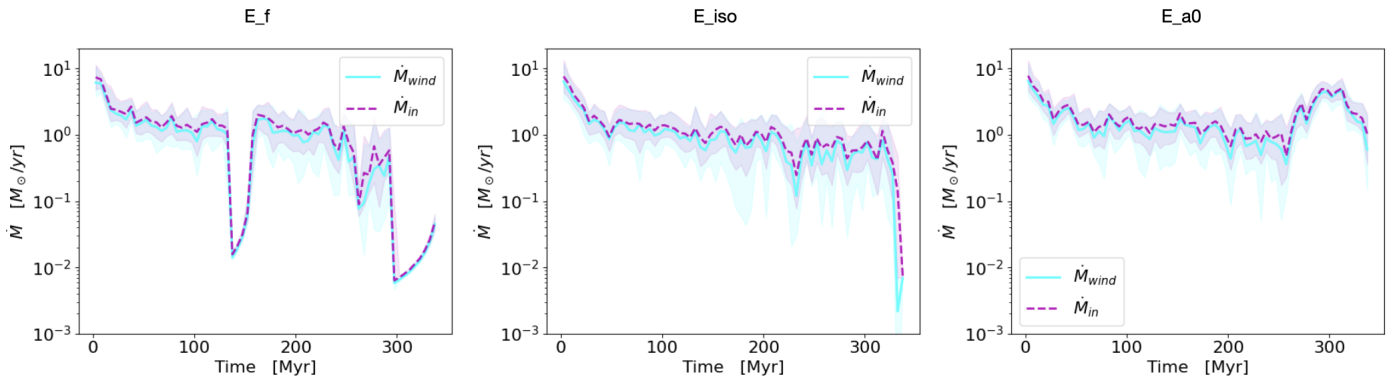


**Fig. 8.** Evolution of the mass inflow rate  $\dot{M}_{in}$  on the subgrid disk and the mass outflow rate  $\dot{M}_w$  ejected in winds for the three **E** simulations. The solid and dashed lines correspond to the median values of these quantities over time bins of 5 Myr, while the shaded regions span from the 16th to the 84th percentiles of  $\dot{M}_{in}$  and  $\dot{M}_w$  within the bins.

central cavity, the AGN wind opening angle and the CGM properties.

### 5.2.1. Star formation rate history

In Figure 11 we show the evolution of the star formation rate (SFR) with time. In order to differentiate the effect of the AGN feedback on nuclear and galactic scales, in the left panel we consider the SFR of the gas particles within 0.5 kpc from the MBH, while in the right panel the SFR of the gas particles within 5 kpc. In both panels, we show results from the simulations sets **C** and **E** and from simulation **NoFb** that with no feedback.

The **NoFb** simulation traces the evolution of the SFR starting from the initial condition with the spinning halo in hydrostatic equilibrium. At this time the SFR is zero, but as soon as the gaseous halo collapses, getting denser and cooler, the SFR grows and peaks at  $\sim 100$  Myr, both on nuclear and galactic scales. At this point, while in the central region the SFR starts to decline, in the whole galaxy stars continue to be formed at a rate of  $100 M_{\odot}/\text{yr} \div 125 M_{\odot}/\text{yr}$ . The switch-on of AGN feedback at  $t_0 = 150$ , in **C** and **E** runs, modifies these trends. In the central 0.5 kpc, the SFR is reduced by a factor of  $\lesssim 2$  in **E** simulations, while it is completely shut off in **C** simulations. The imprint of AGN feedback on galactic scales is less marked: in **E**-simulations the SFR within 5 kpc is not appreciably altered, except for a  $\lesssim 20\%$  decrease during the first  $\sim 50$  Myr of AGN

activity, and a burst of SFR at the end of **E\_iso** due to a clump in a spiral arm, whereas it diminishes by a factor of  $\lesssim 2$  in **C** runs. Overall, these trends do not show any significant dependence on the AGN radiation angular pattern, except for **C** simulations at galactic scale. In this case, we see that the more isotropic the luminosity angular pattern is, the more the SFR is suppressed, due to the increase of wind-ISM coupling. However, this appears as a second order effect and the impact of AGN feedback on the SFR is mainly driven by the AGN luminosity, rather than by its angular pattern.

### 5.2.2. The size of the central cavity

The trends seen in the SFR history are closely related to those seen in the size of the central cavity cleared by AGN feedback. Here the cavity size is measured as the radius  $R_{cav}$  of the sphere centered in the MBH containing a gas mass equal to the MBH mass. Figure 12 shows that in the simulation without feedback this quantity is initially (at  $t_0$ ) about 50 pc and overall grows up to  $\sim 100$  pc. In simulations with AGN feedback, AGN winds tends to push the gas away from the MBH, lowering the gas density in its surroundings and thus increasing  $R_{cav}$ . Such an increase is modest in **E** simulations, by a factor less than 2, while it is about an order of magnitude larger in **C** simulations. In this second case, we can distinguish a dependence of the cavity size with the feedback radiation

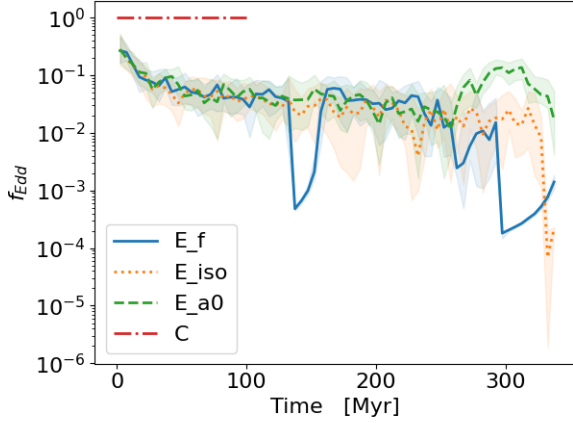


**Fig. 9.** Evolution of  $f_{\text{Edd}}$  in **E** and **C** simulations. The lines correspond to the median values of  $f_{\text{Edd}}$  over time bins of 5 Myr, while the shaded regions represent the fluctuations within the bins from the 16-th to 84-th percentiles.

angular pattern, where a more isotropic pattern results in a larger cavity.

As for the SFR, the cavity size seems to be determined at first order by the disk luminosity and only for high (Eddington) luminosities (**C** runs) by the radiation angular pattern, at least partially. In addition, the increase in the cavity size with disk luminosity and with disk radiation angular pattern mirrors what we found for the SFR, i.e., larger cavities are associated with lower SFRs. This suggests that star formation suppression in the galaxy nuclear region occurs via gas removal caused by AGN winds.

### 5.2.3. The outflow opening angle

Now we show how we measure the opening angle of the region within which the SFR is maintained below  $1 \text{ M}_{\odot}/\text{yr}$ , which provides information about the anisotropy (or angular amplitude) of the bipolar outflow. In order to compute this quantity, we first determined, at any time  $t$ , the SFR angular profile  $\text{SFR}(\theta; t)$ , where  $\theta$  is the polar angle from the galaxy axis<sup>4</sup>. For all simulations,  $\text{SFR}(\theta; t) \approx 10^{-2} \div 10^{-1} \text{ M}_{\odot}/\text{yr}$  for small  $\theta$  – that is, perpendicular to the galaxy disk plane – and rapidly increases at  $\theta \gtrsim \pi/3$ , reaching  $\approx 10 \div 10^2 \text{ M}_{\odot}/\text{yr}$  for  $\theta \lesssim \pi/2$  – that is, in the galactic disk midplane. Given this trend, we define  $\theta_{\star}$  as the angle below which the  $\text{SFR}(\theta; t) < 1 \text{ M}_{\odot}/\text{yr}$ . Then, the larger  $\theta_{\star}$ , the wider the angular region where the outflow manages to keep the SFR below our threshold of  $1 \text{ M}_{\odot}/\text{yr}$ . In this sense,  $\theta_{\star}$  measures the outflow semiopening angle.

In Figure 13, we show how  $\theta_{\star}$  evolves in our simulations and we notice a trend similar to that of  $\text{SFR}(t)$  and  $R_{\text{cav}}(t)$ . Indeed,  $\theta_{\star}(t) \gtrsim \pi/3$  in **NoFb** simulation, then becomes larger in **E** simulations and increases further in **C** runs. No particular trend of  $\theta_{\star}$  is seen with the feedback radiation angular pattern, except for the final part of **C** simulations, which suggest that  $\theta_{\star}$  is larger for more isotropic radiation angular patterns. Therefore, similarly to what we discussed for  $\text{SFR}(t)$  and  $R_{\text{cav}}(t)$ , the disk luminosity, more than its angular pattern, determines the angular amplitude of the outflow, measured as the ability of AGN winds to hamper the SFR at large polar angles.

<sup>4</sup> We defined  $\text{SFR}(\theta; t)$  as the sum of the SFR of all gas particles with polar coordinate  $\theta_i \in [\theta - \Delta\theta/2, \theta + \Delta\theta/2]$ , or  $\pi - \theta_i$  in the same interval, and within a distance of 5 kpc from the MBH. We used  $\Delta\theta = \pi/40$ .

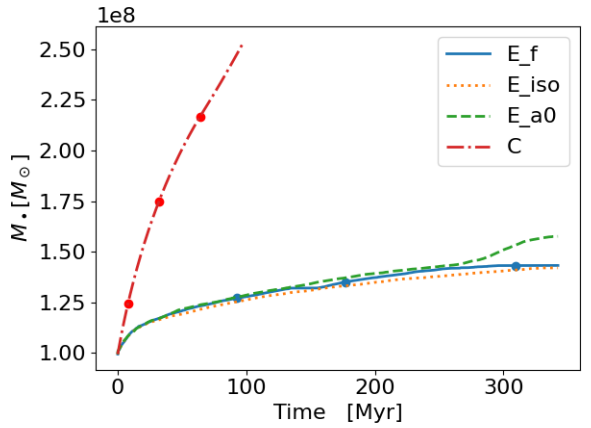
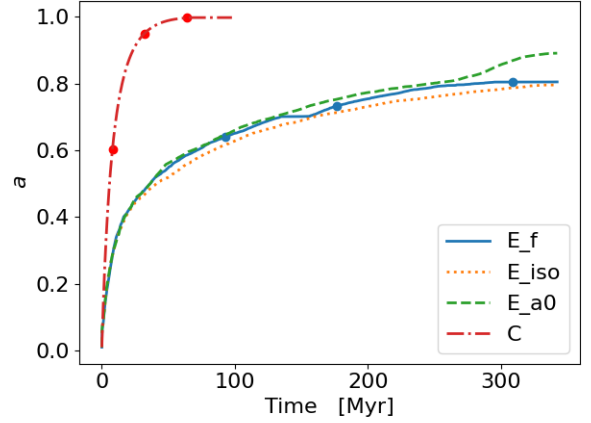


**Fig. 10.** MBH spin and mass growth in **E** and **C** simulations. The red and blue bullet points mark the instants corresponding to the snapshots shown in Figures 5 and 6.

### 5.2.4. The impact on the CGM

While on galactic ( $\sim 10 \text{ kpc}$ ) scales there is a mild or absent dependence of the outflow opening angle on the AGN radiation anisotropy, this is not the case if we look at the larger CGM ( $\sim 100 \text{ kpc}$ ) scales, where an imprint of the feedback anisotropy on the CGM temperature and entropy can be appreciated.

In Figure 14 we show the time averages of the CGM temperature and entropy (left and right of each panel respectively) for the three simulations in the set **E**. Entropy is computed as  $K = k_{\text{B}} T n_e^{-2/3}$  and the time averages only consider snapshots up to 180 Myr from  $t_0$  in order to avoid boundary condition effects caused by the finite size of the sampled halo. Fig. 14 emphasizes that while the opening angle of the outflow on a small scale does not seem to be affected by the anisotropy of the radiation emitted by the AGN, on a larger scale, the more isotropic the radiation angular pattern, the larger the volume fraction of the CGM that is affected by the outflow. This in turn can reflect in the outflow ability to prevent cooling flows on the galaxy and thus on the galaxy cold gas growth and its star formation history on longer timescales. Despite these effects on the energetics of the gas in the CGM, the radial density profile is not affected by feedback anisotropy, as illustrated in Figure 15, where the time averages of these profiles for the **E** simulations are shown.

We provide more details on the CGM energetic balance in Appendix B.

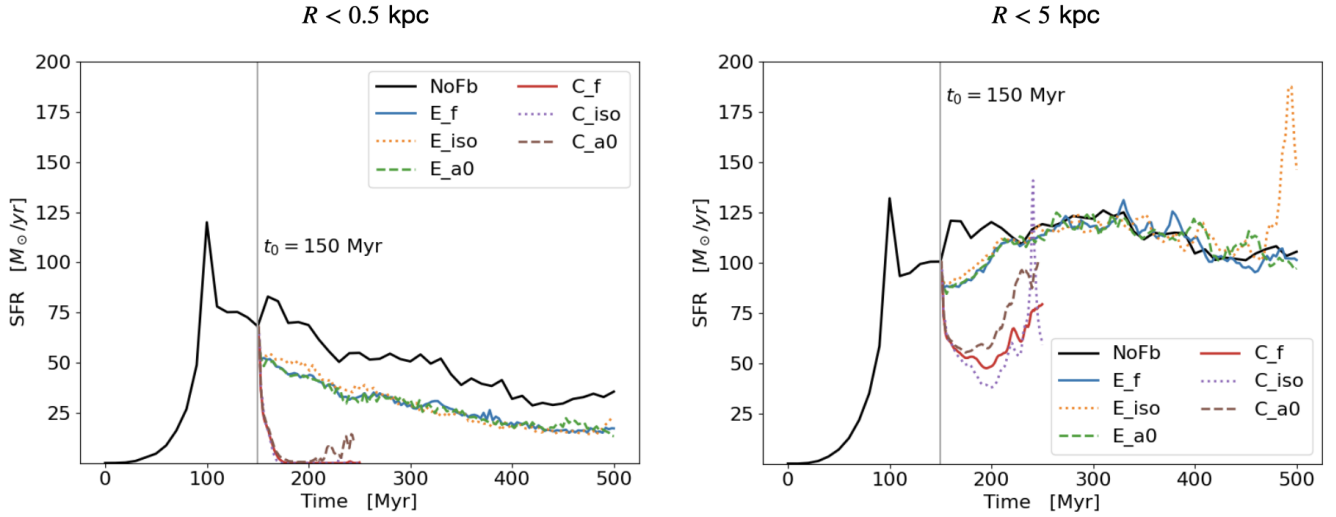


**Fig. 11.** Star formation rate in the nuclear region (left) and at galactic scale (right) for **E**, **C**, and **NoFb** simulations. Here,  $t = 0$  corresponds to the initial condition with the spinning gaseous halo in hydrostatic equilibrium and  $t_0 = 150$  Myr (when AGN feedback is turned on) is marked with a gray vertical line.

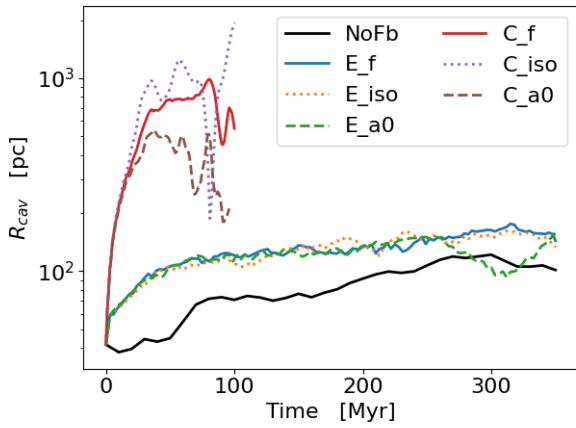


**Fig. 12.** Evolution of the central cavity size in **E**, **C**, and **NoFb** simulations.

## 6. Summary and Discussion

In this study, we investigated the role that spin-dependent anisotropy of AGN winds (Ishibashi et al. 2019; Ishibashi 2020) has in shaping the evolution of MBHs and their host galaxies. To this purpose, we implemented – in the code GIZMO – a subgrid model for AGN feedback that takes into account the spin dependence of feedback anisotropy, linking and integrating existing modules for MBH accretion and spin evolution (Cenci et al. 2021) and AGN wind (Torrey et al. 2020). In doing so, we assumed that the AGN disk radiation couples with gas at the disk (subgrid) scale, completely transferring its momentum. In this way, the nuclear wind that is launched inherits the luminosity angular pattern of the impinging radiation, which is set by the MBH spin. We initially tested our novel implementation by following the propagation of an AGN-wind-driven outflow into a homogeneous medium, and we compared the results against simple analytical models. We then considered an isolated galaxy setup, where the galaxy is thought to be formed from the collapse of a spinning gaseous halo, and there we studied the impact of AGN feedback on the MBH and galaxy evolution. We considered different prescriptions for the MBH accretion rate – that is, constant and equal to the Eddington rate, or self-consistently

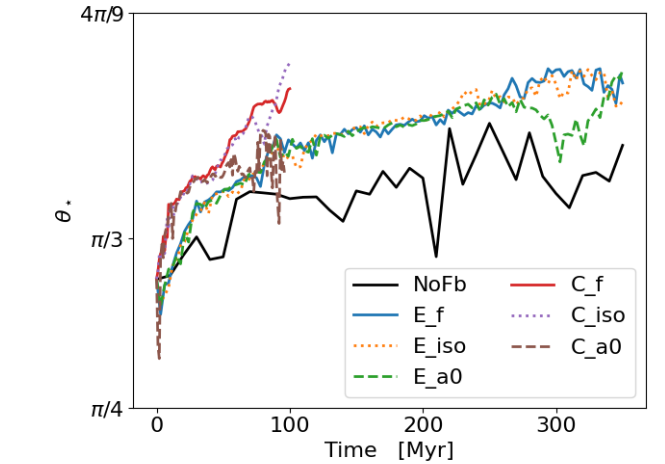


**Fig. 13.** Evolution of the outflow semiopening angle in **E**, **C**, and **NoFb** simulations.

evolving according to the resolved gas inflow onto the MBH. We also considered different degrees of anisotropy of the angular pattern of the launched AGN wind.

The most relevant results of our work can be summarized as follows:

- MBH feedback and fueling are tightly intertwined. On the one hand, the AGN wind affects the gas reservoir that feeds the MBH and, on the other hand, gas flowing onto the MBH supplies material and powers the wind. The disk–wind system is a complex, self-regulating system (Fiore et al. 2024). We find that whether or not we account for such self-regulated evolution makes a crucial difference. In our simulations with an evolving MBH accretion rate, the AGN luminosity, initially set equal to Eddington  $L_{\text{Edd}} = 1.2 \cdot 10^{46}$  erg/s, drops down by between one and two orders of magnitude to  $\approx 6 \cdot 10^{44}$  erg/s, precisely because the AGN feedback limits the inflow that powers itself. Such reduced luminosity corresponds to an Eddington factor of  $f_{\text{Edd}} \sim 0.05$ , which is consistent with what is estimated in Seyfert galaxies (Ho 2009). Such a decrease in luminosity implies both a much slower MBH growth and a much weaker impact of the AGN

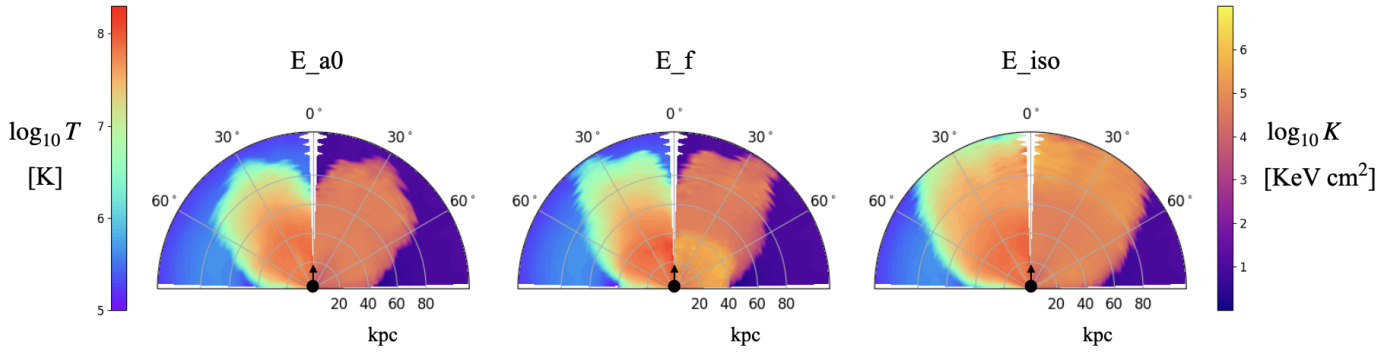


**Fig. 14.** Polar plots of the time averages of CGM temperature and entropy for **E** simulations. Time averages are taken considering snapshots up to 180 Myr from  $t_0$ .

on the host when compared with simulations with a constant Eddington MBH accretion rate. This highlights the importance of self-consistently evolving MBH accretion and feedback.

- Once MBH accretion is allowed to evolve, we find that AGN feedback has a limited impact on the host galaxy, except for the central  $\approx$ kpc-scale region. A smaller,  $\approx$ 100 pc cavity is cleared around the AGN. At the same time, the SFR is approximately halved within the inner 0.5 kpc, while it remains at values typical of inactive galaxies on larger scales. In other words, our simulations indicate that isolated disk galaxies may be able to host luminous AGN activity without undergoing any significant star formation suppression on larger galaxy scales. We emphasize that due to the simulated timescales, the star formation suppression witnessed in our simulations is the result of the AGN wind ejection of the existing ISM, while star formation suppression owing to CGM heating – which prevents cooling and accretion flow onto the galaxy – is at most mildly captured, as such processes unfold on longer, approximately gigayear timescales. Our results agree with many observational studies that find no systematic signature of AGN feedback on the host galaxy SFR (Rosario et al. 2013; Scholtz et al. 2020; Smirnova-Pinchukova et al. 2022; Lammers et al. 2023). In addition, Lammers et al. (2023) noted that AGNs, despite not showing evidence of galaxy-wide quenching, have a significantly suppressed central ( $\sim$ kpc scale) SFR, lying up to a factor of 2 below those of the control inactive galaxies, in agreement with our findings. These results suggest that the integrated effect of secular AGN feedback, which is traced by the MBH mass rather than an instantaneous AGN-driven outflow, is required to significantly affect SF on galactic scales. In other words, the instantaneous AGN luminosity is not a proxy for the cumulative impact of AGN feedback on SF (Bluck et al. 2023). In addition, we recall that, in addition to AGN feedback, other physical processes can be responsible for suppression of SF in the nuclear region; for example, the presence of bars (Gavazzi et al. 2015).
- The impact of AGN feedback on the host galaxy and on MBH growth is primarily determined by AGN disk luminosity rather than by its angular pattern. We find that MBHs accreting with a constant Eddington rate corresponding to a bolometric luminosity of  $L \sim 1.2 \cdot 10^{46}$  erg/s are capable of clearing kpc-scale cavities, suppressing SF by a factor of two on a galactic scale, and driving outflows with large – between  $\sim\pi/3$  and  $\pi/2$  – semiopening angles. For lower luminosities,  $L \sim 6 \cdot 10^{44}$ , which are achieved once self-regulation is allowed, such effects are milder and restricted to the nuclear

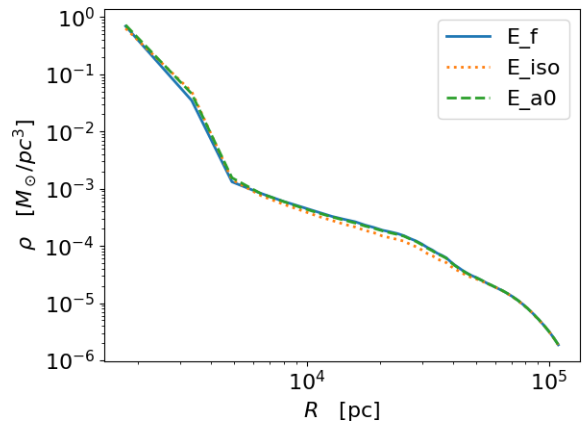


**Fig. 15.** Time averages of the density radial profile of the CGM for the **E** simulations.

region. This is consistent with Torrey et al. (2020), who find that increasing luminosity allows further growth of the central cavity and suppression of SFR.

- Conversely, the imprint of the AGN luminosity angular pattern on the MBH–galaxy evolution is less marked, and can be appreciated only in cases with high (Eddington) constant accretion rates, in which the AGN impact is stronger overall. For maximally anisotropic  $\sim \cos \theta$  angular patterns (our **a0** simulations), most of the wind momentum and energy are funneled in the MBH spin direction – which is perpendicular to the galaxy disk – without significantly affecting the host galaxy. With more isotropic angular patterns, such as those occurring for higher MBH spin because of relativistic light bending, a larger fraction of the wind energy and momentum is distributed perpendicular to the spin – that is, into the galactic disk –, yielding a higher coupling between the wind and the galaxy ISM. Indeed, in our simulations with Eddington accretion, we observe that AGNs with isotropic luminosity more efficiently suppress the host SFR – that is, by up to a factor of two compared to the maximally anisotropic case – and more easily sweep away gas in the nuclear region, clearing cavities up to ten times larger. However, in simulations with smaller ( $f_{\text{Edd}} \sim 0.05$ ) accretion rates, differences in the response of the galaxy to different AGN radiation anisotropies are negligible, with the exception of the CGM, on which the impact of the outflow shows small but appreciable differences with the AGN feedback angular pattern. As a consequence, we expect the spin-dependent anisotropy of AGN radiation to be relevant in those scenarios

characterized by high and prolonged MBH accretion episodes and by a high opening angle of the ISM disk as seen by the central MBH, as both features would increase the wind–galaxy coupling and make the galaxy response more sensitive to the radiation angular pattern. These conditions might be satisfied during galaxy mergers, where large amounts of gas are funneled into the galactic nucleus, resulting in elevated MBH accretion rates and quasi-isotropic central gas geometries, or in high-redshift galaxies characterized by thick disks and by MBH accretion rates close to the Eddington limit over long periods of time (e.g., Di Matteo et al. 2017; Barai & de Gouveia Dal Pino 2019; Lupi et al. 2019, 2022).

- The spin growth itself is influenced by the AGN angular pattern. Given a constant accretion rate, the spin growth naturally slows down due the distance of the ISCO from the MBH becoming smaller with increasing spin. In addition, as the spin becomes larger, both AGN luminosity and its isotropy increase and make the AGN feedback more capable of reducing the inflow on the MBH itself, further delaying its spin and mass growth. We see a hint of this trend in our simulations with self-regulated accretion, noting that more isotropic angular patterns yield slower MBH mass and spin growths; nevertheless, this effect appears negligible in our simulations. In this respect, we might speculate that, because of the angular pattern anisotropy, high-redshift slowly spinning MBHs might more easily attain accretion rates above the Eddington limit, as they would be less prone to hinder accretion flows in the AGN disk equatorial plane via winds (Lupi et al. 2016), but also because the efficiency of the jets – potentially suppressing super-Eddington accretion rates – is lower for lower MBH spins (Regan et al. 2019; Massonneau et al. 2023).

While in this paper we discuss the role of the spin-dependent anisotropy of AGN winds in the context of isolated disk galaxies, we note that this effect might be crucial in other astrophysical scenarios where AGN feedback intervenes, such as the pairing and migration of MBH binaries (e.g., del Valle & Volonteri 2018; Bollati et al. 2023). Due to our simplified modeling, there are indeed a number of caveats that we have to keep in mind when interpreting our results:

- Our accretion model does not include the geometrically thick, radiatively inefficient accretion mode that occurs below  $\lesssim f_{\text{Edd}} \sim 0.01$ . For such low accretion rates, the disk is still modeled as an  $\alpha$ -disk. Moreover, once the disk enters such a low accretion regime, it becomes prone to launching a jet, a phenomenon not included in our model. Due to these limitations, we are not able to capture any transition from quasar to jet mode with its possible repercussion on the host galaxy and MBH evolution. Nonetheless, this should not occur frequently given that, in our simulations,  $f_{\text{Edd}} > 0.01$  most of the time.
- The coupling coefficient  $\tau = \dot{M}_w v_w / (L/c)$  between AGN radiation and gas is assumed to be constant and equal to one. All the momentum transfer is assumed to take place at the disk (unresolved) scale with the launch of the AGN wind. In a more realistic model, the radiation–gas coupling should evolve according to the ionization level of the gas, and a fraction of the AGN radiation should be allowed to escape the unresolved disk scale and interact directly with the resolved ISM gas, exerting radiation pressure on it (Costa et al. 2018; Barnes et al. 2018). This would require radiation-hydrodynamics simulations, something we leave for future work.

- We did not model stellar winds and supernovae which, together with AGN feedback, contribute to driving galactic outflows, especially in dwarf galaxies (Koudmani et al. 2022), and to regulating the amount of gas present in the central region of a galaxy, thus further modulating the AGN fueling (Dubois et al. 2015; Anglés-Alcázar et al. 2017b). These effects would add a further layer of complexity – beyond the scope of this paper – that is important in order to understand the detailed interaction between star formation, MBH growth and feedback, and the overall co-evolution of MBHs and galaxies.
- The multiphase structure of the ISM is not resolved, but is evolved in a subgrid fashion according to the (Springel & Hernquist 2003) model. An explicit modeling of the inhomogeneous and clumpy ISM structure (Hopkins et al. 2018; Lupi et al. 2019; Marinacci et al. 2019) is beyond the scope of our novel investigation of spin-dependent feedback.

We plan to address some of the caveats listed above in future work aimed at developing and enriching the subgrid model presented in this paper. Similarly, we plan to use this model to study other astrophysical regimes relevant for black holes evolution.

*Acknowledgements.* We acknowledge the CINECA award under the ISCRA initiative, for the availability of high-performance computing resources and support (project number HP10CAKAY4). The analyses reported in this work have been mainly performed using pynbody (Pontzen et al. 2013). The data underlying this article will be shared on reasonable request to the corresponding author.

## References

- Akerman, N., Tonnesen, S., Poggianti, B. M., Smith, R., & Marasco, A. 2023, *ApJ*, **948**, 18
- Anglés-Alcázar, D., Davé, R., Faucher-Giguère, C.-A., Özel, F., & Hopkins, P. F. 2017a, *MNRAS*, **464**, 2840
- Anglés-Alcázar, D., Faucher-Giguère, C.-A., Quataert, E., et al. 2017b, *MNRAS*, **472**, L109
- Barai, P., & de Gouveia Dal Pino, E. M. 2019, *MNRAS*, **487**, 5549
- Barai, P., Murante, G., Borgani, S., et al. 2016, *MNRAS*, **461**, 1548
- Barausse, E. 2012, *MNRAS*, **423**, 2533
- Bardeen, J. M., & Petterson, J. A. 1975, *ApJ*, **195**, L65
- Bardeen, J. M., Press, W. H., & Teukolsky, S. A. 1972, *ApJ*, **178**, 347
- Barnes, D. J., Kannan, R., Vogelsberger, M., & Marinacci, F. 2018, *MNRAS*, submitted [arXiv:1812.01611]
- Berti, E., & Volonteri, M. 2008, *ApJ*, **684**, 822
- Blandford, R. D., & Znajek, R. L. 1977, *MNRAS*, **179**, 433
- Bluck, A. F. L., Piotrowska, J. M., & Maiolino, R. 2023, *ApJ*, **944**, 108
- Bollati, F., Lupi, A., Dotti, M., & Haardt, F. 2023, *MNRAS*, **520**, 3696
- Bourne, M. A., & Nayakshin, S. 2013, *MNRAS*, **436**, 2346
- Bower, R. G., Benson, A. J., & Crain, R. A. 2012, *MNRAS*, **422**, 2816
- Bullock, J. S., Dekel, A., Kolatt, T. S., et al. 2001, *ApJ*, **555**, 240
- Bustamante, S., & Springel, V. 2019, *MNRAS*, **490**, 4133
- Campitiello, S., Ghisellini, G., Sbarato, T., & Calderone, G. 2018, *A&A*, **612**, A59
- Cenci, E., Sala, L., Lupi, A., Capelo, P. R., & Dotti, M. 2021, *MNRAS*, **500**, 3719
- Choi, E., Ostriker, J. P., Naab, T., & Johansson, P. H. 2012, *ApJ*, **754**, 125
- Cicone, C., Brusa, M., Ramos Almeida, C., et al. 2018, *Nat. Astron.*, **2**, 176
- Costa, T., Sijacki, D., & Haehnelt, M. G. 2014, *MNRAS*, **444**, 2355
- Costa, T., Rosdahl, J., Sijacki, D., & Haehnelt, M. G. 2018, *MNRAS*, **473**, 4197
- Costa, T., Pakmor, R., & Springel, V. 2020, *MNRAS*, **497**, 5229
- Croton, D. J., Springel, V., White, S. D. M., et al. 2006, *MNRAS*, **365**, 11
- Curtis, M., & Sijacki, D. 2016, *MNRAS*, **463**, 63
- Davé, R., Anglés-Alcázar, D., Narayanan, D., et al. 2019, *MNRAS*, **486**, 2827
- del Valle, L., & Volonteri, M. 2018, *MNRAS*, **480**, 439
- Di Matteo, T., Springel, V., & Hernquist, L. 2005, *Nature*, **433**, 604
- Di Matteo, T., Croft, R. A. C., Feng, Y., Waters, D., & Wilkins, S. 2017, *MNRAS*, **467**, 4243
- Dotti, M., Volonteri, M., Perego, A., et al. 2010, *MNRAS*, **402**, 682
- Dubois, Y., Volonteri, M., Silk, J., et al. 2015, *MNRAS*, **452**, 1502
- Dubois, Y., Beckmann, R., Bournaud, F., et al. 2021, *A&A*, **651**, A109

- Dyson, J. E., & Williams, D. A. 1997, *The Physics of the Interstellar Medium*, 2nd edn. (Bristol: Institute of Physics Publishing)
- Famidakis, N., Baugh, C. M., Benson, A. J., et al. 2011, *MNRAS*, **410**, 53
- Faucher-Giguère, C.-A., & Quataert, E. 2012, *MNRAS*, **425**, 605
- Ferrarese, L., & Merritt, D. 2000, *ApJ*, **539**, L9
- Fiacconi, D., Sijacki, D., & Pringle, J. E. 2018, *MNRAS*, **477**, 3807
- Fiore, F., Gaspari, M., Luminari, A., Tozzi, P., & de Arcangelis, L. 2024, *A&A*, **686**, A36
- Fluetsch, A., Maiolino, R., Carniani, S., et al. 2019, *MNRAS*, **483**, 4586
- Fluetsch, A., Maiolino, R., Carniani, S., et al. 2021, *MNRAS*, **505**, 5753
- Gavazzi, G., Consolandi, G., Dotti, M., et al. 2015, *A&A*, **580**, A116
- Grudić, M. Y., Guszejnov, D., Hopkins, P. F., Offner, S. S. R., & Faucher-Giguère, C.-A. 2021, *MNRAS*, **506**, 2199
- Häring, N., & Rix, H.-W. 2004, *ApJ*, **604**, L89
- Harrison, C. M. 2017, *Nat. Astron.*, **1**, 0165
- Hartwig, T., Volonteri, M., & Dashyan, G. 2018, *MNRAS*, **476**, 2288
- Henden, N. A., Puchwein, E., Shen, S., & Sijacki, D. 2018, *MNRAS*, **479**, 5385
- Henriques, B. M. B., White, S. D. M., Thomas, P. A., et al. 2015, *MNRAS*, **451**, 2663
- Hirschmann, M., Dolag, K., Saro, A., et al. 2014, *MNRAS*, **442**, 2304
- Ho, L. C. 2009, *ApJ*, **699**, 626
- Hopkins, P. F. 2015, *MNRAS*, **450**, 53
- Hopkins, P. F., & Quataert, E. 2011, *MNRAS*, **415**, 1027
- Hopkins, P. F., Torrey, P., Faucher-Giguère, C.-A., Quataert, E., & Murray, N. 2016, *MNRAS*, **458**, 816
- Hopkins, P. F., Wetzel, A., Kereš, D., et al. 2018, *MNRAS*, **477**, 1578
- Ishibashi, W. 2020, *MNRAS*, **495**, 2515
- Ishibashi, W., & Fabian, A. C. 2015, *MNRAS*, **451**, 93
- Ishibashi, W., Fabian, A. C., & Reynolds, C. S. 2019, *MNRAS*, **486**, 2210
- Kauffmann, G., & Haehnelt, M. 2000, *MNRAS*, **311**, 576
- King, A. 2003, *ApJ*, **596**, L27
- King, A. 2005, *ApJ*, **635**, L121
- King, A., & Pounds, K. 2015, *ARA&A*, **53**, 115
- Klein, A., Barausse, E., Sesana, A., et al. 2016, *Phys. Rev. D*, **93**, 024003
- Koo, B.-C., & McKee, C. F. 1992, *ApJ*, **388**, 93
- Kormendy, J., & Ho, L. C. 2013, *ARA&A*, **51**, 511
- Koudmani, S., Sijacki, D., & Smith, M. C. 2022, *MNRAS*, **516**, 2112
- Lammers, C., Iyer, K. G., Ibarra-Medel, H., et al. 2023, *ApJ*, **953**, 26
- Li, L.-X., Zimmerman, E. R., Narayan, R., & McClintock, J. E. 2005, *ApJS*, **157**, 335
- Liao, S., Chen, J., & Chu, M. C. 2017, *ApJ*, **844**, 86
- Luminari, A., Tombesi, F., Piconcelli, E., et al. 2020, *A&A*, **633**, A55
- Lupi, A., Haardt, F., Dotti, M., et al. 2016, *MNRAS*, **456**, 2993
- Lupi, A., Volonteri, M., Decarli, R., et al. 2019, *MNRAS*, **488**, 4004
- Lupi, A., Volonteri, M., Decarli, R., Bovino, S., & Silk, J. 2022, *MNRAS*, **510**, 5760
- Lynden-Bell, D. 1969, *Nature*, **223**, 690
- Magorrian, J., Tremaine, S., Richstone, D., et al. 1998, *AJ*, **115**, 2285
- Marinacci, F., Sales, L. V., Vogelsberger, M., Torrey, P., & Springel, V. 2019, *MNRAS*, **489**, 4233
- Massonneau, W., Volonteri, M., Dubois, Y., & Beckmann, R. S. 2023, *A&A*, **670**, A180
- Mercedes-Feliz, J., Anglés-Alcázar, D., Hayward, C. C., et al. 2023, *MNRAS*, **524**, 3446
- Miller, M. J., & Bregman, J. N. 2013, *ApJ*, **770**, 118
- Miller, M. J., & Bregman, J. N. 2015, *ApJ*, **800**, 14
- Murray, N., Quataert, E., & Thompson, T. A. 2005, *ApJ*, **618**, 569
- Navarro, J. F., Frenk, C. S., & White, S. D. M. 1997, *ApJ*, **490**, 493
- Nesvadba, N. P. H., Boulanger, F., Lehnert, M. D., Guillard, P., & Salome, P. 2011, *A&A*, **536**, L5
- Pontzen, A., Roškar, R., Stinson, G., & Woods, R. 2013, Astrophysics Source Code Library [record ascl:1305.002]
- Pounds, K. A., Reeves, J. N., King, A. R., et al. 2003, *MNRAS*, **345**, 705
- Reeves, J. N., O'Brien, P. T., Braito, V., et al. 2009, *ApJ*, **701**, 493
- Regan, J. A., Downes, T. P., Volonteri, M., et al. 2019, *MNRAS*, **486**, 3892
- Reynolds, C. S. 2021, *ARA&A*, **59**, 117
- Richings, A. J., & Faucher-Giguère, C.-A. 2018, *MNRAS*, **474**, 3673
- Rosario, D. J., Santini, P., Lutz, D., et al. 2013, *ApJ*, **771**, 63
- Sala, L., Cenci, E., Capelo, P. R., Lupi, A., & Dotti, M. 2021, *MNRAS*, **500**, 4788
- Sazonov, S. Y., Ostriker, J. P., & Sunyaev, R. A. 2004, *MNRAS*, **347**, 144
- Schaye, J., Crain, R. A., Bower, R. G., et al. 2015, *MNRAS*, **446**, 521
- Scholtz, J., Harrison, C. M., Rosario, D. J., et al. 2020, *MNRAS*, **492**, 3194
- Sesana, A., Barausse, E., Dotti, M., & Rossi, E. M. 2014, *ApJ*, **794**, 104
- Shakura, N. I., & Sunyaev, R. A. 1973, *A&A*, **24**, 337
- Smirnova-Pinchukova, I., Husemann, B., Davis, T. A., et al. 2022, *A&A*, **659**, A125
- Soltan, A. 1982, *MNRAS*, **200**, 115
- Springel, V., & Hernquist, L. 2003, *MNRAS*, **339**, 289
- Springel, V., Di Matteo, T., & Hernquist, L. 2005, *ApJ*, **620**, L79
- Su, K.-Y., Hopkins, P. F., Bryan, G. L., et al. 2021, *MNRAS*, **507**, 175
- Thompson, T. A., Fabian, A. C., Quataert, E., & Murray, N. 2015, *MNRAS*, **449**, 147
- Tombesi, F., Meléndez, M., Veilleux, S., et al. 2015, *Nature*, **519**, 436
- Torrey, P., Hopkins, P. F., Faucher-Giguère, C.-A., et al. 2020, *MNRAS*, **497**, 5292
- Tozzi, G., Cresci, G., Marasco, A., et al. 2021, *A&A*, **648**, A99
- Tremmel, M., Karcher, M., Governato, F., et al. 2017, *MNRAS*, **470**, 1121
- Veilleux, S., Maiolino, R., Bolatto, A. D., & Aalto, S. 2020, *A&ARv*, **28**, 2
- Vogelsberger, M., Genel, S., Sijacki, D., et al. 2013, *MNRAS*, **436**, 3031
- Vogelsberger, M., Genel, S., Springel, V., et al. 2014, *MNRAS*, **444**, 1518
- Volonteri, M., Madau, P., Quataert, E., & Rees, M. J. 2005, *ApJ*, **620**, 69
- Volonteri, M., Habouzit, M., & Colpi, M. 2021, *Nat. Rev. Phys.*, **3**, 732
- Weaver, R., McCray, R., Castor, J., Shapiro, P., & Moore, R. 1977, *ApJ*, **218**, 377
- Weinberger, R., Springel, V., Hernquist, L., et al. 2017, *MNRAS*, **465**, 3291
- Williamson, D., Hönig, S., & Venanzi, M. 2019, *ApJ*, **876**, 137
- Zubovas, K., & King, A. 2012, *ApJ*, **745**, L34
- Zubovas, K., & Maskeliūnas, G. 2023, *MNRAS*, **524**, 4819
- Zubovas, K., & Nayakshin, S. 2012, *MNRAS*, **424**, 666

## Appendix A: BH accretion implementation

Here we review more in detail the subgrid model for accretion and spin evolution we employed. In [Cenci et al. \(2021\)](#), the MBH particle is meant to represent a structured, sub-resolution system consisting of a MBH surrounded by an unresolved, warped accretion  $\alpha$ -disk ([Shakura & Sunyaev 1973](#)). The MBH particle is completely characterized by its dynamical mass  $M_{\bullet, \text{dyn}}$ ,<sup>5</sup> whereas the sub-resolution, proper MBH by its mass  $M_{\bullet}$  and the dimensionless spin-parameter  $a$ . The unresolved accretion disk is specified by its mass  $M_{\alpha}$ , its total angular momentum  $\mathbf{J}_{\alpha}$ , and its accretion rate  $\dot{M}_{\text{acc}} = f_{\text{Edd}} \dot{M}_{\text{Edd}}$ , where  $\dot{M}_{\text{Edd}} = 4\pi GM_{\bullet} m_p / (\sigma_T \eta c)$  is the Eddington accretion rate,  $m_p$  the proton mass,  $\sigma_T$  the Thomson scattering cross-section.

The time evolution of the MBH mass is governed by the accretion rate from the disk on the MBH  $\dot{M}_{\text{acc}}$ , whereas the mass of the unresolved disk evolves according to the mass inflow  $\dot{M}_{\text{in}}$  from resolved scales, the mass outflow  $\dot{M}_{\text{w}}$  and  $\dot{M}_{\text{acc}}$ :

$$\dot{M}_{\bullet} = (1 - \eta) \dot{M}_{\text{acc}}, \quad (\text{A.1})$$

$$\dot{M}_{\alpha} = \dot{M}_{\text{in}} - \dot{M}_{\text{acc}} - \dot{M}_{\text{w}}. \quad (\text{A.2})$$

Similarly, the MBH angular momentum  $\mathbf{J}_{\bullet} = aGM_{\bullet}^2/c$  evolves due to the accretion from the disk and the Bardeen-Patterson torque  $\mathbf{T}_{\text{BP}}$  ([Bardeen & Petterson 1975](#)) that the MBH and the warped disk exert on each other. The disk angular momentum evolution  $d\mathbf{J}_{\alpha}/dt$  is set equal and opposite to  $d\mathbf{J}_{\bullet}/dt$ , according to angular momentum conservation, plus terms that account for the exchange of angular momentum with the resolved environment through winds  $\dot{\mathbf{J}}_{\text{w}}$  and inflows  $\dot{\mathbf{J}}_{\text{in}}$ :

$$\frac{d\mathbf{J}_{\bullet}}{dt} = \text{sign}(\mathbf{J}_{\bullet} \cdot \mathbf{J}_{\alpha}) \Lambda_{\text{ISCO}} \dot{M}_{\text{acc}} - \mathbf{T}_{\text{BP}} \quad (\text{A.3})$$

$$\frac{d\mathbf{J}_{\alpha}}{dt} = -\frac{d\mathbf{J}_{\bullet}}{dt} + \dot{\mathbf{J}}_{\text{in}} - \dot{\mathbf{J}}_{\text{w}}. \quad (\text{A.4})$$

Here  $\Lambda_{\text{ISCO}}$  is the specific angular momentum of the gas at the disk innermost stable circular orbit (ISCO) and  $\mathbf{T}_{\text{BP}}$  is modelled as in [Fiacconi et al. \(2018\)](#). The angular momentum carried by the wind is given by

$$\dot{\mathbf{J}}_{\text{w}} dt = \mathbf{J}_{\alpha} \left( 1 - \left( 1 - \frac{\dot{M}_{\text{w}} dt}{M_{\alpha}} \right)^{7/5} \right), \quad (\text{A.5})$$

which is computed assuming that the wind arises as ejecta from the outskirts of the disk i.e.  $\dot{\mathbf{J}}_{\text{w}} dt = \int_{R'}^{R_{\text{out}}} \Sigma \sqrt{GM_{\bullet} R} 2\pi R dR$  where  $R'$  satisfies  $\dot{M}_{\text{w}} dt = \int_{R'}^{R_{\text{out}}} \Sigma 2\pi R dR$ , with  $\Sigma \propto R^{-3/4}$  being the disk surface density and  $R_{\text{out}}$  the disk external radius, defined as the radius where the disk becomes self-gravitating.

The accretion in the disk  $\dot{M}_{\text{acc}}$  is self-consistently evolved according to the evolution of the subgrid quantities determined by Eqs. (A.1)-(A.4). In particular, at any given MBH timestep  $f_{\text{Edd}}$  is computed as

$$f_{\text{Edd}} \approx 0.76 \left( \frac{\eta}{0.1} \right) \left( \frac{M_{\alpha}}{10^4 M_{\odot}} \right)^5 \left( \frac{M_{\bullet}}{10^6 M_{\odot}} \right)^{-47/7} \left( \frac{a|\mathbf{J}_{\alpha}|}{3|\mathbf{J}_{\bullet}|} \right)^{-25/7}, \quad (\text{A.6})$$

see ([Fiacconi et al. 2018](#)) for its derivation. Below we discuss more in detail how the inflows  $\dot{M}_{\text{in}}$  and  $\dot{\mathbf{J}}_{\text{in}}$  are computed.

<sup>5</sup> The dynamical mass is that used in the computation of the gravitational force.

### A.1. Accretion from resolved scales on the subgrid disk

The accretion rate  $\dot{M}_{\text{in}}$  from resolved scales on the subgrid disk is estimated based on the properties of the gas particles within the MBH smoothing kernel  $h_{\bullet}$ , which is defined as a spherical region centered on the MBH enclosing a given effective number of particles  $N_{\text{ngb}}$  capped to a maximum size  $R_{\text{max}}$ . In particular, the inflow  $\dot{M}_{\text{in}}$  is estimated through a modified Bondi-Hoyle prescription that accounts for the angular momentum of gas in the BH kernel, as proposed by [Tremmel et al. \(2017\)](#). The argument suggested by [Tremmel et al. \(2017\)](#), similarly to the classical Bondi-Hoyle derivation, is based on the definition of a characteristic accretion radius  $R_{\text{acc}}$ , relative to the MBH, within which gas is bound to the MBH, and from which the accretion rate is computed as  $\dot{M}_{\text{in}} \sim \pi R_{\text{acc}}^2 \rho v$ , where  $v$  is the characteristic velocity of gas nearby the MBH and  $\rho$  its the density. The accretion radius is defined as the radial distance at which the gravitational potential of the MBH balances the internal and bulk energetics of the gas, but differently from the classical Bondi-Hoyle derivation, the computation is carried out in the reference frame of rotating gas, where the gas angular momentum provides an effectively lower gravitational potential:  $U_{\text{eff}}(r) = -GM_{\bullet}/r + \Lambda(r)^2/2r^2$ , where  $\Lambda(r)$  is the angular momentum per unit mass of the gas at distance  $r$  from the MBH. If the dominant motion of the gas is rotational rather than a bulk flow, the energy balance reduces to the requirement that the effective potential balances with the thermal energy of the gas, i.e.  $U_{\text{eff}} \sim c_s^2/2$ . This allows to get  $R_{\text{acc}}$  and then, assuming that the characteristic velocity of gas can be approximated as  $v \sim c_s$ , one obtains

$$\dot{M}_{\text{in}} = \frac{4\pi(GM_{\bullet})^2 \rho c_s}{(v_{\varphi}^2 + c_s^2)^2}, \quad (\text{A.7})$$

where  $v_{\varphi} \equiv \Lambda(r)/r$  encapsulates the amount of angular momentum support the gas has on the smallest resolved scales. Numerically, we compute  $v_{\varphi}$  by estimating the specific angular momentum  $\Lambda$  of gas close to the MBH (i.e. prone to accrete) as the ratio between the kernel weighted averages of angular momentum and mass of particles in the MBH kernel. Then, assuming that angular momentum on the larger scales is conserved once the gas reaches the smallest resolved scale, we set  $v_{\varphi} = |\Lambda|/R_{\text{in}}$ , where  $R_{\text{in}} \equiv h_{\bullet}/3$  is a proxy of the smallest resolved scale in the MBH kernel<sup>6</sup>. Then, if  $v_{\varphi} < v_{\text{bulk}}$ , where  $v_{\text{bulk}}$  is the mass averaged velocity of gas in the MBH kernel, we adopt the usual Bondi-Hoyle formula ([Springel et al. 2005](#); [Di Matteo et al. 2005](#); [Cenci et al. 2021](#))

$$\dot{M}_{\text{in}} = \frac{4\pi(GM_{\bullet})^2 \rho}{(v_{\text{bulk}}^2 + c_s^2)^{3/2}}, \quad (\text{A.8})$$

otherwise Eq. (A.7). Both in Eq. (A.7) and (A.8)  $\rho$  and  $c_s$  are computed as mass-weighted averages on the gas particles within the MBH kernel. As an example, in Fig. A.1 we show the evolution of the ratio between  $\dot{M}_{\text{in}}$  and the corresponding classical Bondi-Hoyle (Eq. A.8) prescription in the simulation **E\_f**. This ratio is always much smaller than one, i.e. Eq. (A.8) is never employed to compute the accretion on the subgrid disk as gas kinematics is dominated by rotation instead of bulk motion. The Bondi-Hoyle accretion is about two orders of magnitude larger than the modified Bondi (Eq. A.7) accretion, in agreement with other works (e.g., [Hopkins & Quataert 2011](#); [Curtis & Sijacki 2016](#); [Tremmel et al. 2017](#); [Akerman et al. 2023](#)), which showed that the classical Bondi-Hoyle accretion has the tendency to

<sup>6</sup> In case  $h_{\bullet}$  reaches its minimum value  $\sim 2.8\epsilon_{\bullet}$ , we have that  $R_{\text{in}} \sim \epsilon_{\bullet}$ .

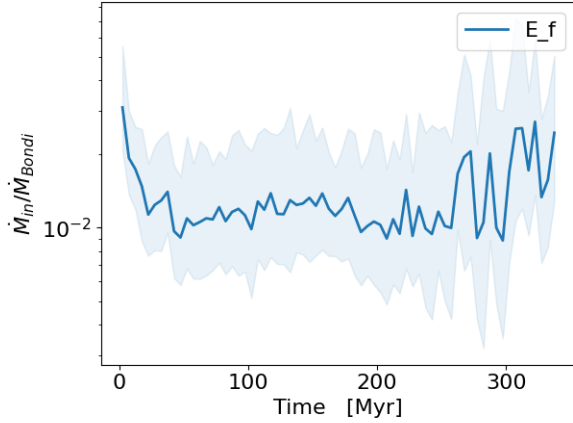


**Fig. A.1.** Ratio between the modified-Bondi accretion rate  $\dot{M}_{\text{in}}$  and the classical Bondi rate in simulation **E\_f**.

overestimate the accretion on the MBH. Once the accretion rate  $\dot{M}_{\text{in}}$  is computed, it is used to update the mass of the subgrid disk, which evolves smoothly over time. Instead, the growth of the MBH particle, i.e. its dynamical mass  $M_{\bullet, \text{dyn}}$ , is performed in a discrete fashion by selecting stochastically the gas particles in the MBH kernel to be accreted, with probability  $p \propto \max[M_{\bullet} + M_{\alpha} - (M_{\bullet, \text{dyn}} + \sum_k^N m_k), 0]$ , where  $m_k$  is the mass of the  $k$ -th gas particle among the  $N$  selected. We remark that both in the computation of the accretion rate  $\dot{M}_{\text{in}}$  and in the stochastic accretion, only nonwind particles are accounted, i.e. particles not spawned from the subgrid disk (see section 3), since such particles are initialized as outflowing and hence they do not contribute to the accretion flow on the MBH.

From the accretion  $\dot{M}_{\text{in}}$  on the subgrid disk, we easily get the accreted angular momentum on the subgrid disk as  $\dot{\mathbf{J}}_{\text{in}} = \dot{M}_{\text{in}} \Lambda dt$ , where  $|\Lambda|$  is limited as in Cenci et al. (2021) in order to account for not resolved processes like shocks and torques that make the accreting gas further loose angular momentum before accreting on the subgrid disk at not resolved scales.

While the subgrid disk mass is capped in order to avoid it from becoming self-gravitating, it is allowed to become zero, i.e. quiescent MBH, due to the accretion on the MBH and wind ejection. Once  $M_{\alpha}$  vanishes, the disk is refilled with probability  $p = (\sum \dot{M}_{\text{in}} dt) / M_{\text{seed}}$ , where  $\sum \dot{M}_{\text{in}} dt$  is the mass inflow collected since the MBH became quiescent and  $M_{\text{seed}}$  is a free parameter ( $10^5 M_{\odot}$  in our simulations). If refilling occurs, the new subgrid disk is initialized with  $M_{\alpha} = \max[M_{\text{seed}}, \sum \dot{M}_{\text{in}} dt]$ ,  $f_{\text{Edd}} = 0.1$ , angular momentum set by Eq. (5) of Cenci et al. (2021) and its direction equal to that of the angular momentum in the MBH kernel.

## A.2. The derivative of $f_{\text{Edd}}$

Here we compute the derivative of  $f_{\text{Edd}}$  and find an approximate expression suitable for interpreting results shown in section 5.1. Starting from Eq. (A.6) and replacing  $a/J_{\bullet} = c/GM_{\bullet}^2$ , the time derivative of  $f_{\text{Edd}}$  reads

$$\begin{aligned} \frac{df_{\text{Edd}}}{dt} &= f_{\text{Edd}} \left( \frac{\dot{\eta}}{\eta} + 5 \frac{\dot{M}_{\alpha}}{M_{\alpha}} + \frac{3}{7} \frac{\dot{M}_{\bullet}}{M_{\bullet}} - \frac{25}{7} \frac{\dot{J}_{\alpha}}{J_{\alpha}} \right) \simeq \\ &\simeq f_{\text{Edd}} \left( \frac{\dot{\eta}}{\eta} + 5 \frac{\dot{M}_{\text{in}} - \dot{M}_{\text{acc}} - \dot{M}_{\text{w}}}{M_{\alpha}} + \frac{3}{7} \frac{(1-\eta)\dot{M}_{\text{acc}}}{M_{\bullet}} \dots \right. \\ &\quad \left. \dots - \frac{25}{7} \frac{\dot{J}_{\text{in}} - \dot{J}_{\bullet} - \dot{J}_{\text{w}}}{J_{\alpha}} \right), \end{aligned} \quad (\text{A.9})$$

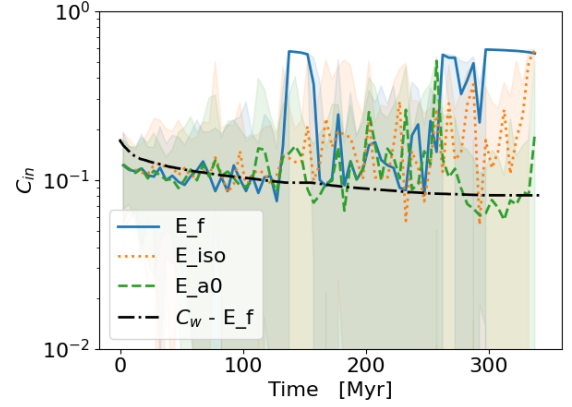


**Fig. A.2.** Coefficients  $C_{\text{in}}$  in **E** simulations. The lines correspond to the median values over time bins of 5 Myr, while the shaded regions span from the 16th to the 84th percentiles over these bins. The coefficient  $C_{\text{w}}$  is also shown for the **E\_f** run.

where in the second row, we plugged in Eqs. (A.1, A.2), and (A.4) in place of  $\dot{M}_{\alpha}$ ,  $\dot{M}_{\bullet}$  and  $\dot{J}_{\alpha}$  and, for Eq. (A.4), we approximated all vectors as lying along the same direction. Eq. (A.9) can be simplified as follows. First, we note that  $-5\dot{M}_{\text{w}}/M_{\alpha} + 25/7\dot{J}_{\text{w}}/J_{\alpha} = 0$ , according to the definition of  $\dot{J}_{\text{w}}$  (Eq. A.5). In other words, the removal of mass and angular momentum from the disk due to the wind ejection does not affect the disk accretion rate. In addition,  $3/7(1-\eta)\dot{M}_{\text{acc}}/M_{\bullet}$  and  $\dot{\eta}/\eta \propto \dot{M}_{\text{acc}}/M_{\bullet}$  are both  $\ll \dot{M}_{\text{acc}}/M_{\alpha}$ , being  $M_{\alpha} \ll M_{\bullet}$ . Similarly, noting that  $\mathbf{T}_{\text{BP}}$  in Eq. (A.3) doesn't affect the spin modulus but only its direction, we can write  $|\dot{J}_{\bullet}/J_{\alpha}| = \Lambda_{\text{ISCO}}/(J_{\alpha}/M_{\alpha}) \cdot \dot{M}_{\text{acc}}/M_{\alpha} \ll \dot{M}_{\text{acc}}/M_{\alpha}$  since the specific angular momentum of gas orbiting at the ISCO is much smaller than the disk total specific angular momentum  $J_{\alpha}/M_{\alpha}$ . In this way, Eq. (A.9) reduces to

$$\frac{df_{\text{Edd}}}{dt} \simeq f_{\text{Edd}} \left( -5 \frac{\dot{M}_{\text{acc}}}{M_{\alpha}} + 5 \frac{\dot{M}_{\text{in}}}{M_{\alpha}} - \frac{25}{7} \frac{\dot{J}_{\text{in}}}{J_{\alpha}} \right). \quad (\text{A.10})$$

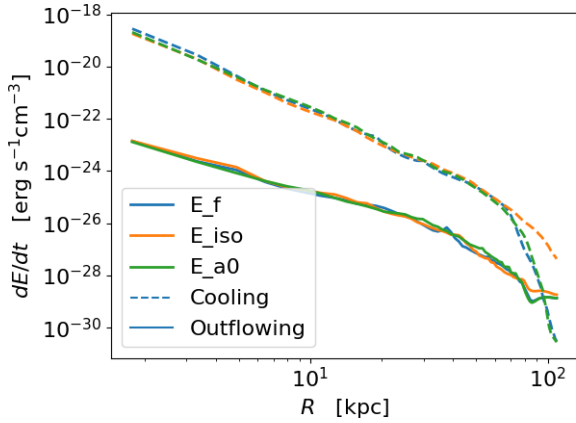
Now, if we write  $\dot{J}_{\text{in}} = \langle \Lambda \rangle \dot{M}_{\text{in}}$  (see Section A.1) and  $\dot{M}_{\text{acc}} = \eta_{\text{w}}^{-1} \dot{M}_{\text{w}}$  (using Eq. 5), we obtain

$$\frac{df_{\text{Edd}}}{dt} \simeq 5f_{\text{Edd}} \left( -\frac{1}{\eta_{\text{w}}} \frac{\dot{M}_{\text{w}}}{M_{\alpha}} + \left( 1 - \frac{5}{7} \frac{\langle \Lambda \rangle}{J_{\alpha}/M_{\alpha}} \right) \frac{\dot{M}_{\text{in}}}{M_{\alpha}} \right). \quad (\text{A.11})$$

This equation points out that the leading terms driving the evolution of  $f_{\text{Edd}}$  are the loss of mass due to accretion, here expressed in terms of  $\dot{M}_{\text{w}}$ , and the replenishment of mass from resolved scales, represented by  $\dot{M}_{\text{in}}$ . If we define the coefficients  $C_{\text{w}} = \eta_{\text{w}}^{-1}$  and  $C_{\text{in}} = (1 - 5\langle \Lambda \rangle / 7(J_{\alpha}/M_{\alpha}))$  we get Eq. (17). For our choice of parameters, being  $v_{\text{w}}/c = 0.01$ , we have that  $C_{\text{w}} = 0.1(\eta/0.1)^{-1}$  is of the same order of  $C_{\text{in}}$ , whose value is shown in Fig. A.2 for the three simulations **E**.

## Appendix B: CGM energetic balance

In this section we discuss more in detail the energetic balance in the CGM, i.e. we compare the cooling luminosity of the gas and the energy flux of the outflow. The cooling luminosity is defined as  $\dot{\epsilon}_{\text{cool}}(r) = \sum_i n_{\text{H},i}^2 \Lambda_{\text{cool},i} / N$ , where  $\Lambda_{\text{cool},i}$  is the total cooling function of the  $i$ -th particle and the sum spans over the  $N$  gas particles in the radial bin  $[r - \Delta R/2, r + \Delta R/2)$ , where we used  $\Delta R = 1.5$  kpc. We defined the energy flux of the outflow as  $\dot{\epsilon}_{\text{outflow}}(r) = \sum_i \rho_i (0.5v_i^2 + u_i) v_{r,i} / N \Delta R$ , where  $v_i$ ,  $u_i$  and  $v_{r,i}$  are the  $i$ -th particle velocity, internal energy and radial velocity. In



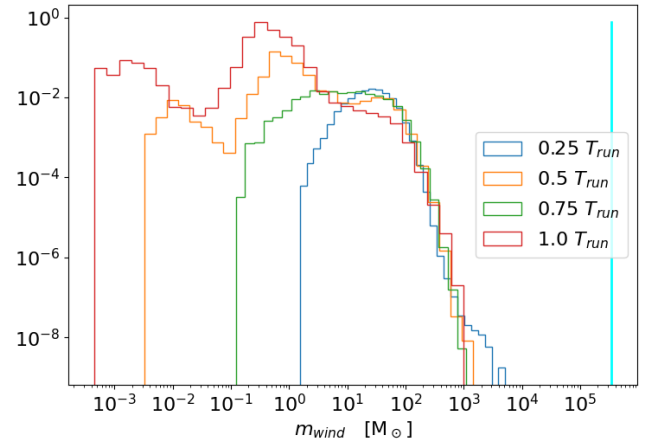
**Fig. B.1.** Time averages of the cooling luminosity (dashed) and outflow energy flux (solid) radial profiles for the **E** simulations. Time averages are taken considering snapshots up to 180 Myr from  $t_0$ .

Fig. B.1 we show the time averages (over the same snapshots accounted in 5.2.4) of these quantities for the **E** simulations.

For each simulation, the location where the two energy rates become comparable roughly coincides with the maximum radius within which the CGM is affected by the outflow, as shown in the Fig. 14. While for anisotropic feedback (**E\_f** and **E\_a0**) this occurs at  $R \sim 100$  kpc, for isotropic feedback (**E\_iso**) the region impacted by the outflow extends beyond the radial range considered.

### Appendix C: Wind particles

In this section we study the mass resolution of wind particles and the location where such particles are merged to nonwind particles for **E\_f** simulation. In Fig. C.1 we show the normalized histograms of the wind particles masses at four snapshots of **E\_f**: at one quarter, one half, three quarters and at the end of the simulation. The vertical cyan line shows the value of the nonwind particle mass resolution. According to this figure, wind particles throughout the simulation have masses orders of magnitude smaller than the initial ISM resolution, reason why we exclude the possibility that at the time of spawning these particles could result in a significant and instantaneous perturbation of the gas density surrounding the MBH. In addition, we considered the location where wind particles are merged into ISM particles. Figure C.2 shows the normalized histogram of the radii where such mergers occur throughout all **E\_f** simulation. It follows that wind particles capture is much more likely to occur within the first few hundreds pc from the MBH, but still takes place up to a distance of  $\sim 10$  kpc.



**Fig. C.1.** Normalized histograms of wind particles masses at four snapshots of **E\_f** simulation. The cyan line indicates the mass of nonwind particles at the beginning of the simulation.

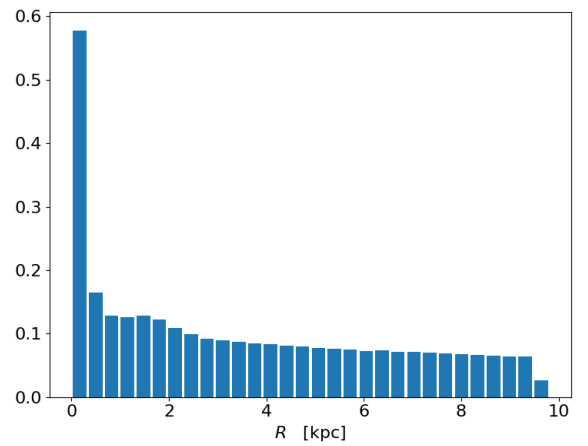


**Fig. C.2.** Normalized histogram of the radii where wind particles merge with ISM particles in **E\_f** simulation.